

# **Cold Fog Amongst Complex Terrain**

Zhaoxia Puo, Eric R. Pardyjak, Sebastian W. Hoch, Ismail Gultepe, A. Gannet Hallar, Alexei Perelet, Rebecca Beal, Gerardo Carrillo-Cardenas, Xin Li, Maria Garcia, Steven Oncley, William Brown, Jeffrey Anderson, Jacquelyn Witte, and Andrei Vakhtin

## **KEYWORDS:**

Boundary layer; Fog; In situ atmospheric observations; Mountain meteorology

**ABSTRACT:** Cold fog forms via various thermodynamic, dynamic, and microphysical processes when the air temperature is less than 0°C. It occurs frequently during the cold season in the western United States yet is challenging to detect using standard observations and is very difficult to predict. The Cold Fog Amongst Complex Terrain (CFACT) project was conceived to investigate the life cycle of cold fog in mountain valleys. The overarching goals of the CFACT project are to 1) investigate the life cycle of cold-fog events over complex terrain with the latest observation technology, 2) improve microphysical parameterizations and visibility algorithms used in numerical weather prediction (NWP) models, and 3) develop data assimilation and analysis methods for current and next-generation (e.g., subkilometer scale) NWP models. The CFACT field campaign took place in Heber Valley, Utah, during January and February 2022, with support from NSF's Lower Atmospheric Observing Facilities (managed by NCAR's Earth Observing Laboratory), the University of Utah, and Ontario Technical University. A network of ground-based and aerial in situ instruments and remote sensing platforms were used to obtain comprehensive measurements of thermodynamic profiles, cloud microphysics, aerosol properties, and environmental dynamics. Nine intensive observation periods (IOPs) explored various mountainous weather and cold-fog conditions. Field observations, NWP forecasts, and large-eddy simulations provided unprecedented data sources to help understand the mechanisms associated with cold-fog weather and to identify and mitigate numerical model deficiencies in simulating winter weather over mountainous terrain. This article summarizes the CFACT field campaign, its observations, and challenges during the field campaign, including real-time fog prediction issues and future analysis.

https://doi.org/10.1175/BAMS-D-22-0030.1

Corresponding author: Zhaoxia Pu, zhaoxia.pu@utah.edu

Supplemental material: https://doi.org/10.1175/BAMS-D-22-0030.2

In final form 15 August 2023

© 2023 American Meteorological Society. This published article is licensed under the terms of the default AMS reuse license. For information regarding reuse of this content and general copyright information, consult the AMS Copyright Policy (<a href="https://www.ametsoc.org/PUBSReuseLicenses">www.ametsoc.org/PUBSReuseLicenses</a>).

AFFILIATIONS: Pu, Hoch, Hallar, Beal, Carrillo-Cardenas, Li, and Garcia—Department of Atmospheric Sciences, University of Utah, Salt Lake City, Utah; Pardyjak and Perelet—Department of Mechanical Engineering, University of Utah, Salt Lake City, Utah; Gultepe—Faculty of Engineering and Applied Science, Ontario Technical University, Oshawa, Ontario, Canada, and Civil and Environmental Engineering and Earth Sciences, University of Notre Dame, Notre Dame, Indiana; Oncley, Brown, and Witte—Earth Observing Laboratory, National Center for Atmospheric Research, Boulder, Colorado; Anderson—Data Assimilation Research Section, National Center for Atmospheric Research, Boulder, Colorado; Vakhtin—Mesa Photonics, LLC, Santa Fe, New Mexico

tmospheric fog is a high-impact weather phenomenon affecting human activities, including aviation, marine and ground transportation, human health, and ecosystems. Fog is the second most likely cause of weather-related aviation accidents behind strong winds (Gultepe et al. 2007a, 2017). Other modes of transportation are also disrupted, with speed restrictions implemented on roads, traffic accidents, and cancellation of ferries. In the United States, between 1995 and 2004, 13,720 people were reported to have been killed in fog-related accidents (Forthun et al. 2006). In India, 10,000 people died in 2017 because of fog-related accidents (Kapoor 2019). Despite the high impact of fog events and the long history of fog research, fog prediction remains a challenge for numerical weather prediction (NWP) (e.g., Kunkel 1984; Bott et al. 1990; Bergot and Guédalia 1994a,b; Pagowski et al. 2004; Tardif and Rasmussen 2007; Bergot et al. 2005; Gultepe et al. 2009; Zhou and Du 2010; Gultepe and Milbrandt 2010; Pu et al. 2016; Chachere and Pu 2018; Price et al. 2018; Smith et al. 2020).

## **Cold Fog Amongst Complex Terrain**

During the cold season, when the air temperature is less than 0°C, cold fog can form via various microphysical processes in different forms (e.g., supercooled water or ice fog) (Gultepe et al. 2009, 2015). Cold-fog events in the western United States have long been noted; the Native American-derived word "pogonip," or ice fog, was reported in an editorial in the American Meteorological Journal in 1892. In another editorial from 1900, the Monthly Weather Review stated that pogonips occurred mostly in the northern part of Colorado, Wyoming, and Montana under clear, dry conditions with strong radiative cooling. Today, ice fog and other forms of cold fog (e.g., supercooled liquid fog) regularly form in high-mountain valleys in the western United States. Major cold-fog types (common in complex terrain) include 1) cold-air-pool fog associated with a deep cold-air pool; 2) ephemeral mountain valley cold fog, often forming just before sunrise, evolving for several hours, and dissipating before midday; and 3) radiative ice fog, occurring in the early morning due to longwave cooling during clear-sky conditions. The variety of its types makes cold fog difficult to understand and predict. Cold fog in the western United States is challenging to detect from standard observations due to its high spatiotemporal variability and the use of instruments that cannot distinguish liquid, frozen, and mixed-phase droplets. Compared with fog in other regions, cold fog in complex terrain is unique and necessary to study for the following reasons:

(i) Temporal and spatial variability. There is significant spatial and temporal variability in cold-fog distribution and frequency in complex terrain, such as valleys in northern Utah (Hodges and Pu 2016). Small-scale heterogeneity leads to serious forecasting

- difficulties when using statistical methods and coarse-resolution numerical models. As a result, a dense observing network and high-resolution NWP models are needed to resolve fog events driven by microscale to mesoscale processes (Pu et al. 2016; Zhang and Pu 2019; Li and Pu 2022).
- (ii) Limited observations. Standard meteorological observations from common observational networks are often sparse and less representative in mountainous regions compared to those in flat terrain due to the high spatial variation natural of the mountainous conditions. Microphysical observations of cold-fog conditions are almost nonexistent in mountainous regions. The representativeness of in situ fog observations, such as visibility measurements in mountain valleys, is also generally poor due to the heterogeneous nature of the terrain and land cover. Some active satellites (e.g., CloudSat, CALIPSO) also have limited capabilities to observe fog due to limitations in their sampling frequencies and coverage, as well as vertical resolution close to the surface (less than 600 m). Other satellite and remote sensing (e.g., radar) observations of clouds are also more uncertain over complex terrain (Colman et al. 2013) and may not be useful when there are high-level clouds (Gultepe et al. 2007b, 2020).
- (iii) Lack of studies. Cold fog in complex terrain has not yet received sufficient attention from the research community (Gultepe et al. 2017). For several decades, most fog experiments in the United States have focused on warm-fog conditions, and most experiments have taken place along the California coast (Noonkester 1979; Leipper 1994; Kloesel 1992). While recent field programs have been conducted in mountainous regions (e.g., PCAPS, Lareau et al. 2013; Perdigão, Fernando et al. 2019; Passy-2015, Paci et al. 2016), they have emphasized processes associated with stable-atmosphere dynamics without focusing on microphysical processes. The Local and Non-local Fog Experiment (LANFEX), emphasized radiation-fog formation in complex terrain but did not focus on cold fog (Price et al. 2018). A pilot cold-fog field experiment was conducted as part of the Mountain Terrain Atmospheric Modeling and Observations (MATERHORN) program in the mountains of Utah (Fernando et al. 2015; Gultepe et al. 2016). Its outcomes were limited due to a lack of microphysical and aerosol measurements as well as limited project designs such as not having a detailed mesoscale network.
- (iv) Uncertainties in numerical models. Compared with forecasts in flat terrain, NWP models perform worse when predicting weather events such as cold fog or gusts in complex terrain, likely due to terrain representation issues in NWP models, complicated interactions between atmosphere processes and near-surface boundary layer physical and dynamical processes (e.g., Liu et al. 2008a,b; Mass et al. 2002; Zhang et al. 2013; Massey et al. 2014; Fernando et al. 2015; Pu 2017), and the lack of studies noted above. Challenges are even greater for cold-fog events (Gultepe et al. 2014), as mountain valley cold fog can form due to various processes, such as radiative cooling, cold-air downslope flows, and mixing processes (Gultepe et al. 2016). These processes are associated with a variety of fog types, thus making cold fog difficult to predict.

Considering the gaps and scientific issues related to cold fog over mountainous terrain, a multidisciplinary group of scientists collaborated to address the scientific issues and problems mentioned above. The Cold Fog Amongst Complex Terrain (CFACT) research program was designed to facilitate an extensive field campaign, data analysis, data assimilation, and modeling studies for cold fog with comprehensive research goals (as stated in the abstract).

### **CFACT field campaign**

The CFACT field campaign took place in Heber Valley, Utah, from 7 January to 23 February 2022, with the intent of observing cold fog, including ice fog conditions. The center of Heber

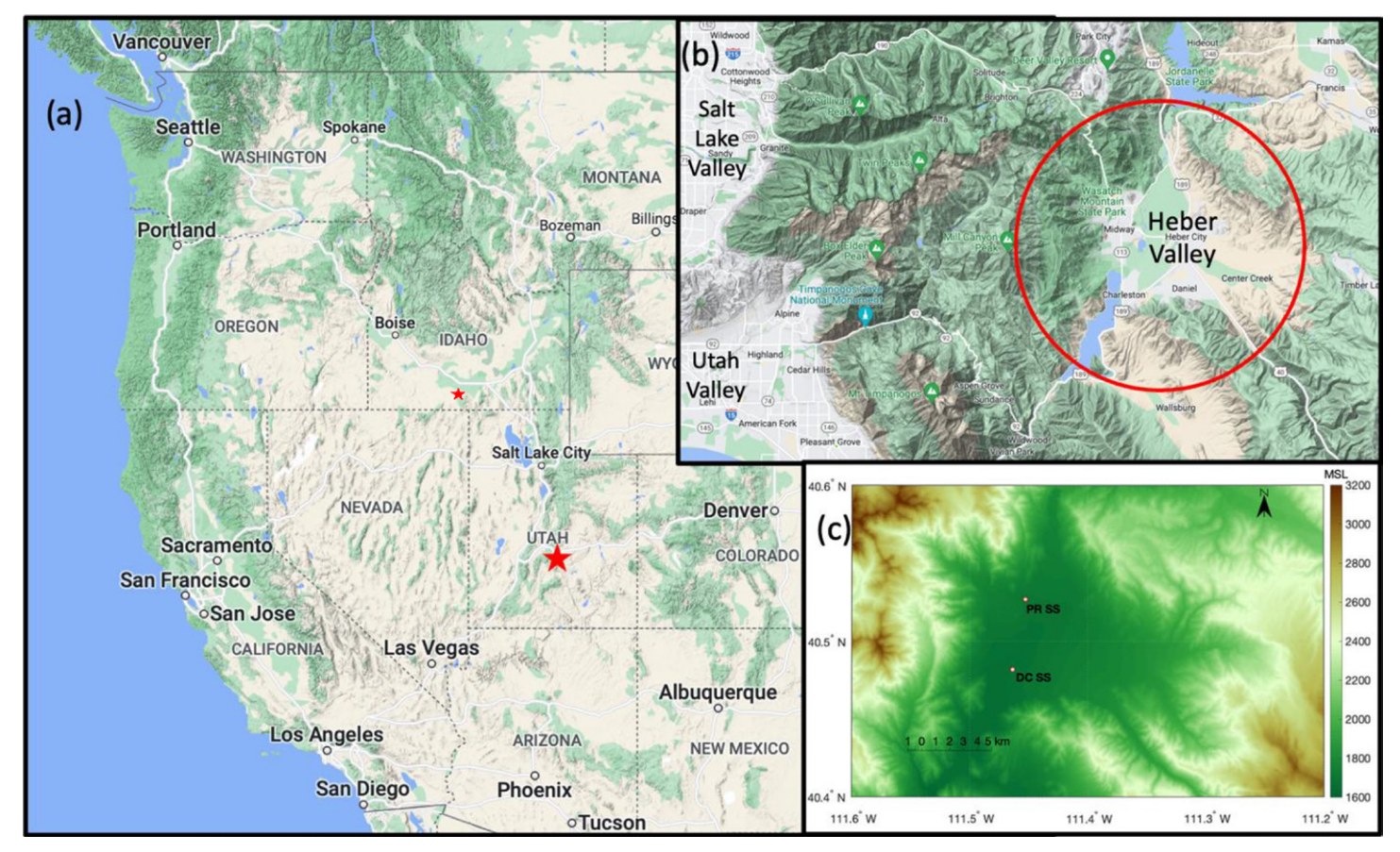


Fig. 1. The location of Heber Valley is indicated by a (a) star and (b) red circle (Google, map data ©2023). (c) Contour plot indicating terrain heights around Heber Valley.

Valley (see Fig. 1) is located at roughly 40.50°N, 111.42°W. This is an alpine valley with agricultural and suburban/urban land cover that is located about 50 km southeast of Salt Lake City. The valley has a diameter of ~16 km and is surrounded by canyons and escarpments. The Provo River runs along the valley floor from Jordanelle Reservoir at the north end of the valley to Deer Creek Reservoir at the southwestern end at an elevation of 1,652 m above mean sea level (MSL). The highest peaks surrounding the valley are roughly 3,500 m MSL and are located to the west and southwest. With the surrounding mountains, slopes, a relatively flat basin, and two reservoirs, Heber Valley is typical of mountain valleys in the North American West and around the world. Heber Valley has statistically significant favorable conditions for all three types of typical fog in mountainous areas: cold-air-pool fog, ephemeral mountain valley cold fog, and radiative ice fog. In particular, Heber Valley exhibits cold nights that trigger ephemeral shallow cold fog, making it an ideal laboratory for studying cold fog in complex terrain.

With support from the NSF Lower Atmospheric Observing Facilities (LAOF), managed by NCAR's Earth Observing Laboratory (EOL), and observing platforms from EOL Integrated Sounding System (ISS) and Integrated Surface Flux System (ISFS) and the University of Utah (UU) as well as Ontario Technical University (OntTecU), the CFACT field deployment included two supersites, nine satellite sites, an aerosol measurement site, a microphysics measurement site, and eight low-cost weather stations (Fig. 2).

CFACT observations emphasize five areas: 1) synoptic, mesoscale, and local weather conditions (SWC): sample the multiscale background weather conditions and local thermodynamic and dynamic conditions; 2) planetary boundary layer (PBL) conditions: characterize the development and evolution of near-surface and atmospheric boundary layer conditions along with energy (heat and radiation) budgets and turbulent fluxes;

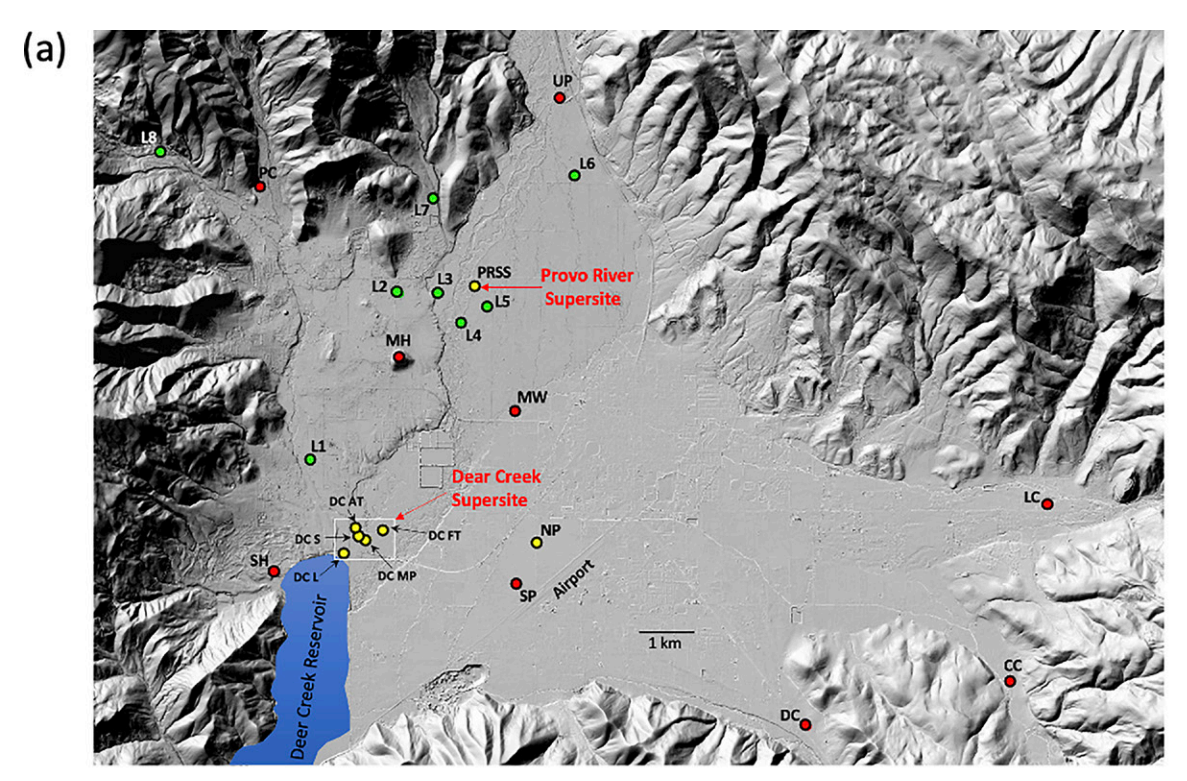




Fig. 2. (a) Locations of CFACT observational sites. Yellow dots denote sites associated with two supersites; red dots indicate the nine NCAR satellite sites. Green dots are low-cost weather stations (LEMS). The Deer Creek Supersite (DC SS) area is marked by a red circle. See Table 1 for a key to the abbreviations. (b) A detailed map of DC SS facilities, including an aerosol trailer, microphysics site, sounding site, flux tower, and lidar site.

3) Earth surface characteristics (ESC): obtain surface snow cover, land surface cover, soil moisture, etc.; 4) microphysics (MP): quantify microphysical properties, ice nuclei number concentration, and size distribution; 5) aerosols (AR): measure aerosol physical and chemical properties, including size distribution and chemical composition. Table S1 in the online supplementary material (https://doi.org/10.1175/BAMS-D-22-0030.2) summarizes the instruments, measurement categories, and platforms to further clarify the function of the instruments listed in Table 1.

Table 1. CFACT experimental site locations and key instrumentation. SS indicates supersite, Sat indicates satellite site, DC is Deer Creek, and PR is the Provo River (as shown in Fig. 1). LW = longwave, MW = microwave, P = nanobarometer pressure, T = temperature, RH = relative humidity, S = snow depth, FWTC = fine-wire thermocouple, Vis = visibility, UVWT = wind vector components and sonic temperature, IRGA = infrared gas analyzer, OPC = optical particle counter, Q = soil moisture content, GCIP = ground-based cloud imaging probe, CDMS = cloud droplet measurement spectrometer, CPD = cloud droplet probe, BCP = backscatter cloud probe, FM120 = fog monitor (droplet spectra), SMPS = scanning mobility particle sizer, CCN = cloud condensation nuclei, GRIMM = aerosol spectrometer, WX = weather conditions.

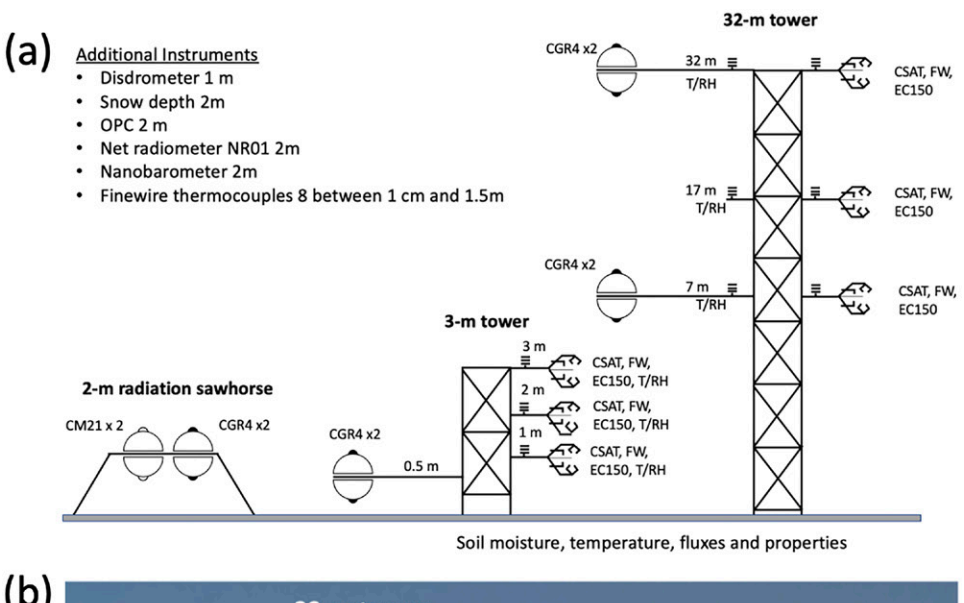
Site	Lat and lon	Elevation (m, MSL)	Key instrumentation
Deer Creek Supersite (DC SS Flux Tower) (DC FT) Main tower	40.490101°N, 111.464737°W	1,659	32-m flux tower: 1, 2, 3, 7, 17, 32 m: <i>T</i> /RH, Sonic UVWT, FWTC, IRGA; 0.5, 2, 7, 32 m: LW-in and LW-out radiation, 2-m <i>P</i> , 2-m four-component radiation, HS, disdrometer, soil <i>T/Q</i> and flux, 2-m OPC, webcam
DC SS Microphysics site (DC MP)	40.488320°N, 111.468143°W	1,659	2-m FM120, 3-m GCIP, 1.25-CDMS, 2-m OPC, 5-m MW/LW scintillometer (Rx), 1.5-m horizontal ceilometer, 5-m Sonic UVWT, 5-m PWD, 5-m radiation, 1.5-m WX, HS
DC SS Sounding Site (DC S)	40.489027°N, 111.470164°W	1,660	Radiosonde soundings, tethered balloon, WX, BCP, UV radiation, CL61 ceilometer, low-cost aerosol
DC SS Aerosol Trailer (DC AT)	40.489940°N, 111.470331°W	1,661	GRIMM, SMPS, CCN, filter measurements
DC SS lidar site (DC L)	40.486426°N, 111.473048°W	1,660	Wind lidar (Leosphere 200S), webcam, GPS water vapor
Provo River Supersite (PR SS)	40.528118°N, 111.445836°W	1,699	32-m flux tower: 1, 2, 3, 7, 17, 32 m: <i>T</i> /RH, Sonic UVWT, FWTC, IRGA; 0.5,2,7,32 m: LW-in and LW-out radiation, 2-m <i>P</i> , 2-m four-component radiation, HS, disdrometer, soil <i>T/Q</i> and flux, 2-m OPC, webcam, wind lidar (Halo Photonics Streamline XR), CL31 and CL51 ceilometers, low-cost aerosol
North Pivot Profiling Site (NP)	40.488229°N, 111.433263°W	1,701	Wind profiler/RASS, WX, CL51 Ceilometer, four-component radiation, disdrometer, low-cost aerosol, webcam
Upper Provo (UP) Satellite	40.55752°N, 111.42852°W	1,740	2-m <i>P</i> , 0.5/2-m <i>T</i> /RH, 2-m Sonic UVWT, 2-m FWTC, 2-m IRGA, 1.5-m four-component radiation, HS, disdrometer, soil <i>T/Q</i> and flux
Center Creek (CC) Satellite	40.466344°N, 111.335625°W	1,865	2-m <i>P</i> , 0.5/2-m <i>T</i> /RH, 2-m Sonic UVWT, 2-m FWTC, 2-m IRGA, 1.5-m four-component radiation, HS, disdrometer, soil <i>T/Q</i> and flux
Lake Creek (LC) Satellite	40.493 671°N, 111.327 65°W	1,873	3-m <i>P</i> , 0.5/2-m <i>T</i> /RH, 3-m Sonic UVWT, 3-m FWTC, 3-m IRGA, 1.5-m four-component radiation, HS, disdrometer, soil <i>T/Q</i> and flux
Daniels Canyon (DC) Satellite	40.459124°N, 111.37758°W	1,809	2-m <i>P</i> , 0.5/2-m <i>T</i> /RH, 2-m Sonic UVWT, 2-m FWTC, 2-m IRGA, 1.5-m four-component radiation, HS, disdrometer, soil <i>T/Q</i> and flux, 1-m Vis
Midway Lane (MW) Satellite	40.508516°N, 111.437739°W	1,679	3-m <i>P</i> , 0.5/2-m <i>T</i> /RH, 3-m Sonic UVWT, 3-m FWTC, 3-m IRGA, 1.5-m four-component radiation, HS, disdrometer, soil <i>T/Q</i> and flux, 1-m Vis
South Pivot (SP) Satellite	40.481 611°N, 111.437 426°W	1,697	2-m <i>P</i> , 0.5/2-m <i>T</i> /RH, 2-m Sonic UVWT, 2-m FWTC, 2-m IRGA, 1.5-m four-component radiation, HS, disdrometer, soil <i>T/Q</i> and flux, 1-m Vis
Soldier Hollow (SH) Satellite	40.483 202°N, 111.487 092°W	1,668	2-m <i>P</i> , 0.5/2-m <i>T</i> /RH, 2-m Sonic UVWT, 2-m FWTC, 2-m IRGA, 1.5-m four-component radiation, HS, disdrometer, soil <i>T/Q</i> and flux, 1-m Vis
Pine Canyon (PC) Satellite	40.543 386°N, 111.490 119°W	1,792	2-m <i>P</i> , 0.5/2-m <i>T</i> /RH, 2-m Sonic UVWT, 2-m FWTC, 2-m IRGA, 1.5-m four-component radiation, HS, disdrometer, soil <i>T/Q</i> and flux
Memorial Hill (MH) Satellite	40.516918°N, 111.461 368°W	1,764	2-m <i>P</i> , 0.5/2-m <i>T</i> /RH, 2-m Sonic UVWT, 2-m FWTC, 2-m IRGA, 1.5-m four-component radiation, HS, 1-m Vis, webcams

**CFACT supersites.** Two supersites were placed in areas with frequent fog formation. As shown in Fig. 1, the Deer Creek Supersite (DC SS) was located near the primary moisture source in the valley (i.e., the Deer Creek Reservoir) and at the lowest elevation, while the Provo River Supersite (PR SS) was sited farther north adjacent to the Provo River where interactions of thermally driven flows with a basin cold-air pool have been shown to modulate fog formation (Hang et al. 2016).

**DC SS.** The DC Supersite consisted of a wide range of equipment designed to measure variables using both in situ and *remote sensing* platforms (Table 1 and Table S1, Fig. 2b),

and can be subdivided into a DC SS flux tower site, a DC SS microphysics site, a DC SS aerosol trailer, a DC SS sounding site, and the DC SS wind lidar (Fig. 2b).

At the DC SS flux tower, in situ meteorological observations included a 32- and 3-m ISFS towers, as well as a radiation measurement sawhorse (see Fig. 3a). Six levels between 1 and



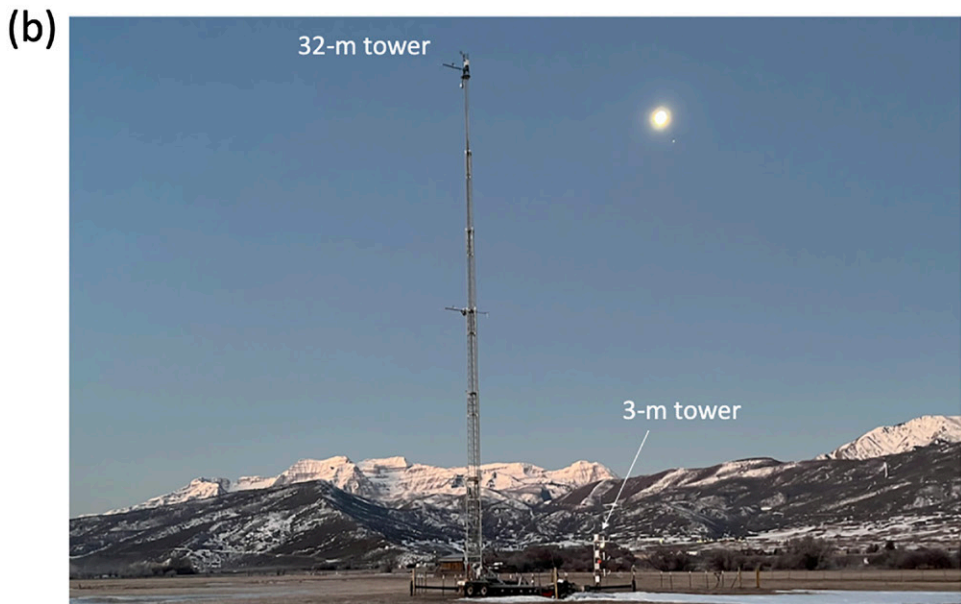




Fig. 3. (a) Illustration of the layout of instruments at the ISFS flux tower with radiative flux divergence measurements deployed at the supersites, (b) photo of the Deer Creek Supersite ISFS 32- and 3-m turbulence and flux divergence towers, and (c) an example satellite site with instrumentation mounted on an ISFS 3-m tower (Daniel Canyon site shown).

 $32\,\mathrm{m}$  were instrumented with fast-response velocity and temperature measurements (sampled at  $20\,\mathrm{Hz}$ ) to capture near-surface turbulence processes, including momentum, heat,  $\mathrm{CO}_2$ , and water-vapor fluxes along with slow-response actively ventilated temperature/relative humidity sensors (1-Hz sampling rate). Longwave incoming and outgoing radiation fluxes were observed at four levels between 0.5 and  $32\,\mathrm{m}$  to infer radiative heating and cooling rates. Two-meter observations of shortwave incoming and outgoing fluxes and an additional four-component net radiometers completed observations of the radiation balance. A nanobarometer collocated with the 2-m flux observations was part of a pressure sensor network (along with those at the satellite sites) designed to understand low-amplitude pressure oscillations associated with gravity waves. Soil heat flux sensors, soil thermal property sensors, soil moisture sensors, and soil thermocouples were also deployed to estimate the ground heat flux. Additional fast-response fine-wire thermocouples were deployed at eight levels with an increasing vertical resolution close to the ground. Additional in situ observations at the flux-tower sites included a disdrometer, an optical particle counter, a snow-depth sensor, and a time-lapse camera (1 min).

At the DC SS profiling site, radiosondes were launched daily at 1615 UTC and eight times per day during intensive observing periods (IOPs), with the sounding schedules depending on the expected fog type (Table 2). A tethered balloon sounding system (TBS) was deployed on a 15-m³ Allsopp Desert Star Helikite to probe the thermodynamic and dynamic structure of the near-surface ABL (up to ~150 m above ground level) and to sample the fog layer for low-wind IOPs. Generally, the TBS was operated in a profiling mode collecting measurements of temperature, pressure, humidity, wind speed, and wind direction. A set of newly available lightweight pyrgeometers and an optical particle counter were flown on the TBS platform to measure radiative flux and liquid water content profiles. A ceilometer monitored the vertical backscatter and linear polarization ratio profile and added a remote sensing platform to the DC SS sounding site. The DC SS wind lidar performed both range—height indicator (RHI) and plan position indicator (PPI) scans to evaluate the temporal and spatial development of the thermally driven flows along the valley's main orientation and tributary valleys. Furthermore, the wind lidar backscatter provided an indication of the extent of patchy fog layers and their motion.

The DC SS Aerosol Trailer. Deployed to quantify the physical and chemical properties of near-surface aerosols (Fig. 4a). Measurements included in situ size-resolved measurements of ambient aerosols from a TSI Inc. Scanning Mobility Particle Sizer (SMPS) and a GRIMM Aerosol Spectrometer [covering particles sizes from 8 nm to 30  $\mu$ m as described in Hallar et al. (2011, 2016)]. The SMPS ran 5-min scans of full-size range, and the GRIMM sampled continuously at 1 Hz. A DMT Cloud Condensation Nuclei (CCN) counter was deployed (e.g., Hallar et al. 2016) and ran continuously sampling at 1 Hz as well. To quantify aerosol chemistry, Teflon filters were collected using Airmetrics MiniVol total air samplers, which sampled ambient air at 5 L min<sup>-1</sup> for particulate matter (PM<sub>10</sub>). One sampler was used to collect PM<sub>10</sub>. The MiniVol was installed at both DC SS and Wasatch State Park. Samples were taken during IOPs at DC SS.

The DC SS microphysics site. This site hosted most of the suite of microphysical instruments (Fig. 4b) including 1) a DMT FM-120 for fog droplet spectral measurements (1–50  $\mu$ m, 15 channels), 2) a DMT ground-based cloud imaging probe (GCIP; 7.5–950  $\mu$ m), 3) a gondola

Table 2. Radiosonde launch schedule times (in MST) for IOPs targeting ephemeral fog and persistent cold-air-pool fog.

		Sounding No.						
	1	2	3	4	5	6	7	8
Ephemeral fog schedule	1415	1615	2215	0015	0215	0415	0715	1015
Persistent cold-pool fog schedule	1415	1615	1915	2215	0115	0415	0715	1015

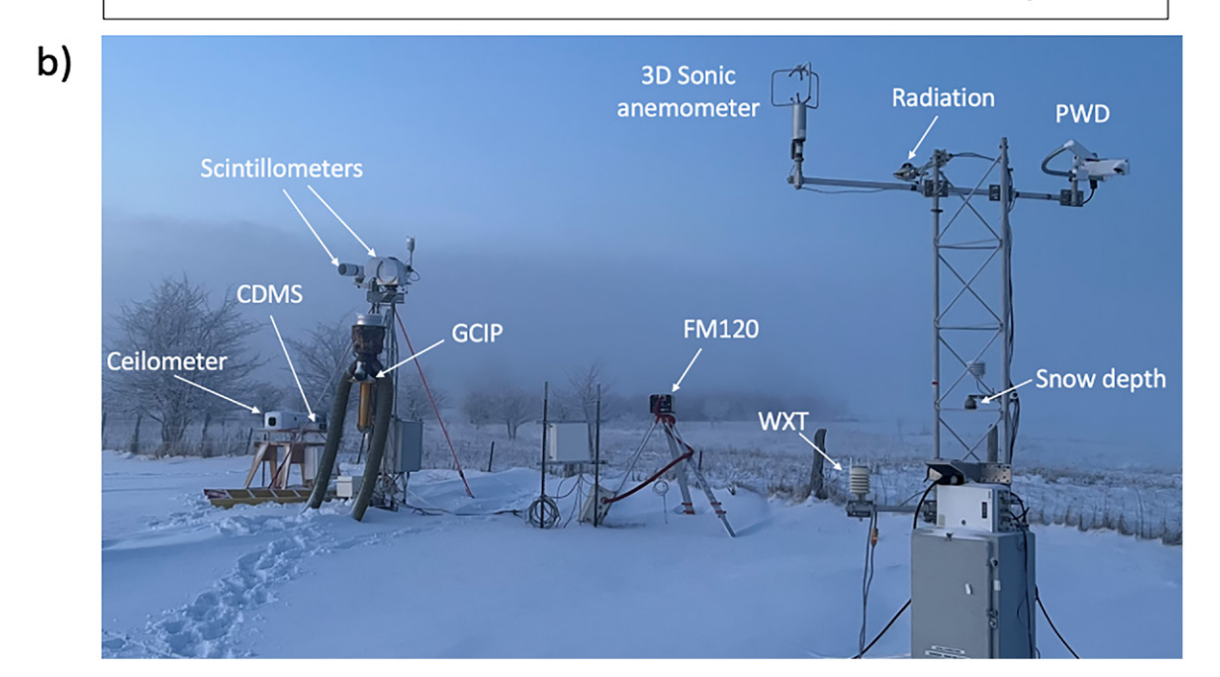


Fig. 4. Photographs of (a) the DC SS Aerosol Trailer and instruments and (b) the microphysics instrument suit with a visibility tower (Gultepe et al. 2021) at the DC Supersite at the beginning of the field campaign.

with both a DMT backscatter cloud and cloud droplet probe (BCP/CDP); 1–75  $\mu$ m for fog droplet spectra that were used at the surface, and 4) a present-weather detector (PWD) for precipitation, fog, visibility measurements, and precipitation type. In addition, a Mesa Photonics' cloud-droplet measurement spectrometer (CDMS) provided droplet size spectral measurements from 10 to 1,000  $\mu$ m for droplets concentration.

A two-wavelength scintillometer system (microwave and near-infrared) with a pathlength of 436 km was installed at the DC SS microphysics site. The path passed the DC SS flux tower site at approximately the center of the path. The system was used to differentiate between fog, liquid, and ice precipitation at scales on the order of 1 km. In parallel to the scintillometer beam, an additional CL31 ceilometer was mounted horizontally to capture spatial heterogeneities of the fog layer. Additional optical particle counters were deployed both at the near and far end of the scintillometer path.

**PR SS.** The PR Supersite (see Fig. 2) deployment consisted of the PR SS flux tower site, which was identical to the DC SS flux tower site (Fig. 3c). In addition, two Vaisala ceilometers (CL31 and CL51) and a CS125 present weather sensor were deployed at the site. A Halo Photonics Streamline XR Doppler wind lidar was deployed at PR SS to better study tributary

flow interactions within Heber Valley at the PR SS. The PR SS provided a second location with continuous high-frequency vertical profile measurements to help understand the spatial variability of the mechanisms modulating the cold-fog processes in Heber Valley.

**Satellite sites.** The purpose of using satellite sites was to better capture the horizontal variability of fog coverage and intensity (Hang et al. 2016; Van Den Bossche and De Wekker 2016) while simultaneously measuring local winds, pressure, and thermodynamic variability for improved modeling, validation, and linking to remote sensing retrievals. The satellite sites were EOL ISFS stations deployed with ~3- or 5-m towers (i.e., Fig. 3c) with fast-response (sampled at 20 Hz) velocity and temperature measurements (sampled at 20 Hz) to capture near-surface turbulence processes including momentum, heat, CO<sub>2</sub>, and water vapor fluxes and two levels of slow-response actively ventilated temperature/relative humidity sensors (1-Hz sampling rate). Most satellite sites also included measurements of visibility using a CS125, while all sites monitored precipitation, the radiation balance, soil heat flux and soil properties (except MH), and snow depth. The South Pivot Satellite Site, to the east of the DC SS was uniquely suited to house additional remote sensing platforms, including the NCAR EOL 449-MHz wind profiler with RASS continuously monitoring a deeper wind and temperature profile and a CL51 ceilometer. Webcams were installed at MH looking toward the south and east.

**LEMS sites.** LEMS are Arduino-based weather stations that measure 2-m wind speed and direction (2D sonic), temperature/relative humidity, air pressure, surface temperature, global radiation, and soil moisture and temperature at two levels (Gunawardena et al. 2018). During the CFACT campaign, eight LEMS (see Fig. 2) were deployed to better understand the heterogeneity of local flows and thermodynamic variables.

### **CFACT IOPs**

The IOPs focused on understanding fog formation, evolution, and dissipation processes. During periods *without* fog, the IOPs emphasized understanding thermally driven circulation and fundamental stable boundary layer processes that are usually important for fog formation. Nine IOPs were conducted (see summary in Table 3) during the CFACT field campaign. Several weak-fog events occurred that were observed by the continuously operating instrumentation but were not part of an IOP. Furthermore, immediately after the main campaign concluded, two fog events were also sampled when much of the DC Supersite instrumentation was still running.

According to the U.S. drought monitor (www.cpc.ncep.noaa.gov/products/Drought/), the western United States has been under drought conditions of various strengths, including northeastern Utah, which has been under severe drought. The 50-day period from 10 January to 28 February 2022 set minimum precipitation records at 59 observation sites across Utah (Clayton et al. 2022). The drought and frequent, persistent high pressure systems over the western United States made conditions unfavorable for persistent fog to form in the Heber Valley during the CFACT campaign. Heber Valley received only 50% of the average precipitation in January, but nearly all of that fell before the beginning of the field campaign, 7 January 2022; February precipitation was only 34% of normal, with snowfall occurring near the end of the CFACT campaign. The Jordanelle and Deer Creek Reservoirs iced over during the field campaign, limiting available water sources. Minimal fog was observed in Heber Valley during January after 7 January 2022. While some fog was observed throughout the Wasatch Front during IOP 3 (19–20 January 2022), no fog occurred in Heber's isolated valley. February experienced several fog events after a snowfall near the end of the field campaign. The complex influence of local terrain and surface conditions on fog formation was observed: During IOP 6, fog was reported at the DC SS but not at the Heber airport despite a separation of only

Table 3. Summary of CFACT fog events and IOPs.

IOP	Date	Fog state	Planned observation type	Notes	Recommended studies based on field observations
IOP 1	11–12 Jan	No fog	Ephemeral fog	No GCIP, no filter samples, poor air quality	Onset and evolution of nighttime inversion under a stable boundary layer
IOP 2	16–17 Jan	No fog	Clear	No TBS, first filter samples, poor air quality	Stable boundary layer with a mature inversion
IOP 3	19–20 Jan	No fog in Heber Valley but fog in surrounding valleys	Ephemeral fog	Fog in surrounding valleys but not in Heber Valley, no TBS, first filter samples	Conditions controlling local fog formation under proper meso- and local-scale environments
	23–24 Jan	Reduced visibility	None	Reduced visibility (below 2 km)	Very weak cold fog
IOP 4	3–4 Feb	lce crystals occurred; fog observed over water body	Ice fog	An ice crystal IOP with ice crystals occurred; shallow fog over the water body close to the DC SS	Ice crystal formation and patchy fog
Fog event	6–7 Feb	0.5 h	None	Very short-lived ephemeral fog event	Ephemeral, spatially heterogeneous fog
IOP 5	9–10 Feb	No fog	Moisture surge	A moisture surge IOP; synoptically forced large-scale advection of moisture; using persistent fog sounding schedule	Moisture advection and transport in the Heber Valley under windy and calm conditions
IOP 6	12–13 Feb	2 h of fog	Ephemeral fog	Quiescent IOP with fog forming around 0300 MST	Typical ephemeral fog formation
Fog event	13–14 Feb	5 h of fog	None	Ephemeral fog	Sporadic ephemeral fog; high RH <sub>ice</sub> at DC SS
IOP 7	17–18 Feb	No fog	Ephemeral fog	Slightly windy and cloudy at start of IOP; cleared up during night; 100% humidity at surface; no fog	No fog formation
IOP 8	18–19 Feb	8 h of fog	Ephemeral fog	Excellent ephemeral IOP with fog starting around 2300 MST and on and off until about 0800 MST	Ephemeral fog case
Fog event	21–22 Feb	1.5 h of fog	None	Snow event	Patchy fog during clearing period snow event
IOP 9	23–24 Feb	5 h of ice fog	Ice fog	Excellent ice fog IOP; more persistent than previous fog IOPs; more widespread fog	Ice fog case
Fog event	25–26 Feb	Morning fog	None	Campaign over but some DC Supersite instrumentation running	Ephemeral fog; cold fog; radiative fog; 3 h of sporadic fog followed by 5 h of persistent fog
Fog event	26–27 Feb	Morning fog	None	Campaign over but some DC Supersite instrumentation running	Ephemeral fog; cold fog; radiative fog

about 2 miles (~3 km). Because of the unusually dry conditions during the CFACT field campaign, observations are suitable primarily for studying ephemeral fog and ice fog events, which are the most difficult to understand and predict. Meanwhile, the variety of CFACT IOPs provided valuable observations for understanding near-surface inversion, ice crystal formation, moisture advection and transportation, and stable boundary layers over complex terrain (see Table 3 for recommended studies), all of which are important areas related to winter weather and fog formation over mountainous regions.

### **Highlights of CFACT observations and initial findings**

We use IOPs 8 and 9 as examples to highlight the preliminary findings with CFACT observations. Figure 5 shows the NOAA GOES-R Advanced Baseline Image (ABI) brightness

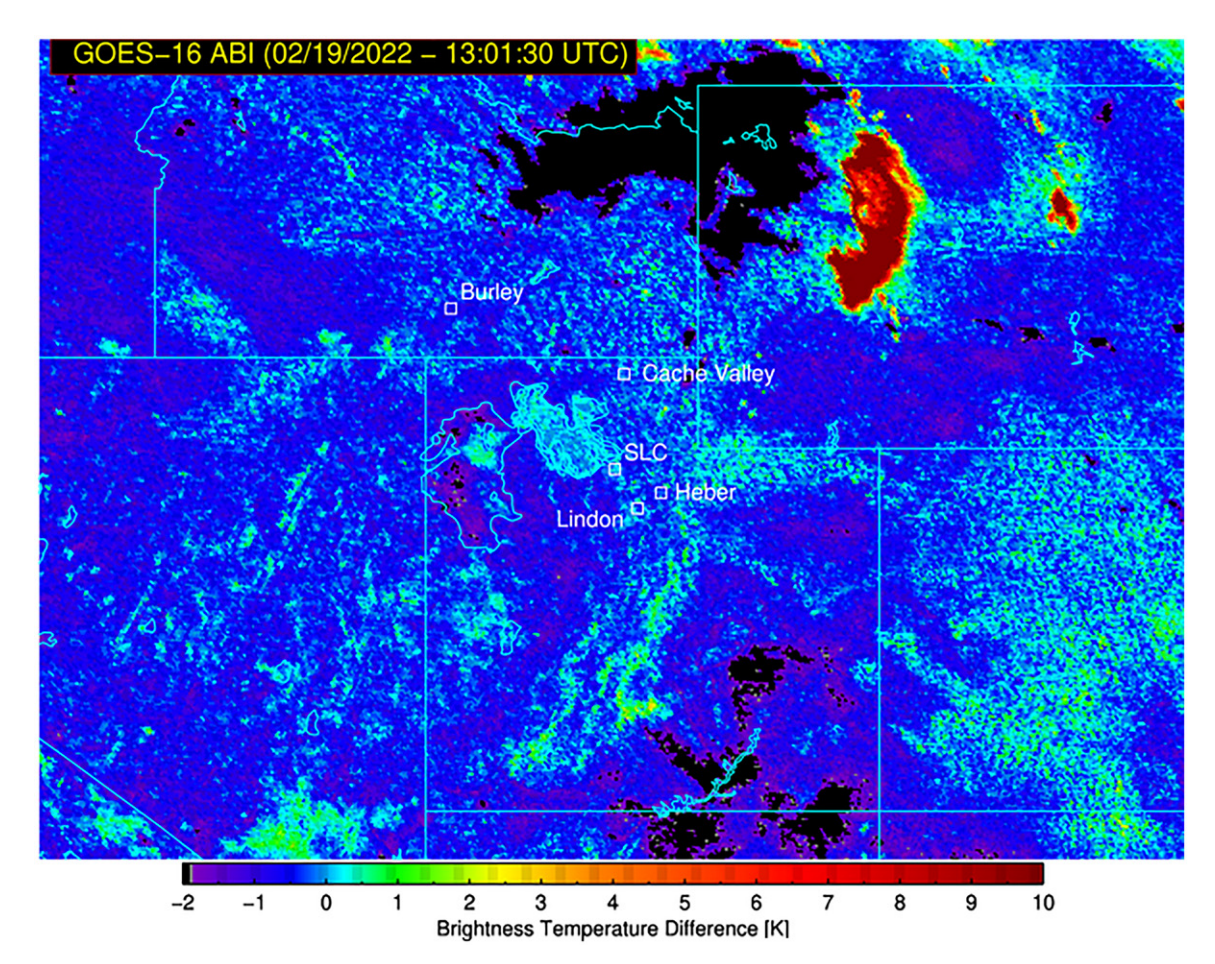


Fig. 5. NOAA GOES-R Advanced Baseline Image (ABI) brightness temperature difference (K), channel 7 (3.9  $\mu$ m) minus channel 14 (11  $\mu$ m), over the upper Intermountain West region of the United States at 1301 UTC 19 Feb 2022. (Figure credit: Cooperative Institute for Meteorological Satellite Studies, University of Wisconsin–Madison.) The image shows pockets of fog throughout Utah and the Intermountain West.

temperature difference over the U.S. Intermountain West at 1301 UTC 19 February 2022 during IOP 8. The figure indicates that patchy fog occurred over Heber Valley at the time. CFACT field observations characterized the formation and evolution of the fog event. Figure 6 illustrates the meteorological conditions, including visibility at the DC SS, as well as relative humidity, temperature, and wind speed observed by the EOL ISFS instruments from the two supersites and the nine satellite sites on 19 February 2022. The visibility observations revealed several low-visibility periods. The corresponding meteorological conditions were also captured by other observations. More notably, the observations differentiated the temporal and spatial variability of near-surface conditions at the different observation sites (Fig. 6) in a small-scale valley with a diameter of  $\sim 16\,\mathrm{km}$ , providing critical high-resolution data to understand variations in weather conditions during fog events. The available observations from the CFACT dense network at a small scale are also expected to be useful for model validation and data assimilation studies at a fine scale.

Figure 7 illustrates the time evolution of meteorological conditions during IOP 8, 18–19 February 2022, from the six tower levels at the DC SS flux tower site. The observations differentiate the larger vertical variations of near-surface meteorological conditions before and during the fog versus those after the fog dissipated. Figure 8 displays potential temperature and mixing ratio profiles in the lowest  $2 \, \text{km}$  AGL from radiosoundings during IOP 8. The basin cold pool is revealed by a persistent capping inversion above  $\sim 1 \, \text{km}$  AGL, confining the diurnal heating cycle to within the lowest  $800 \, \text{m}$  AGL. The mixing ratio profile indicates that

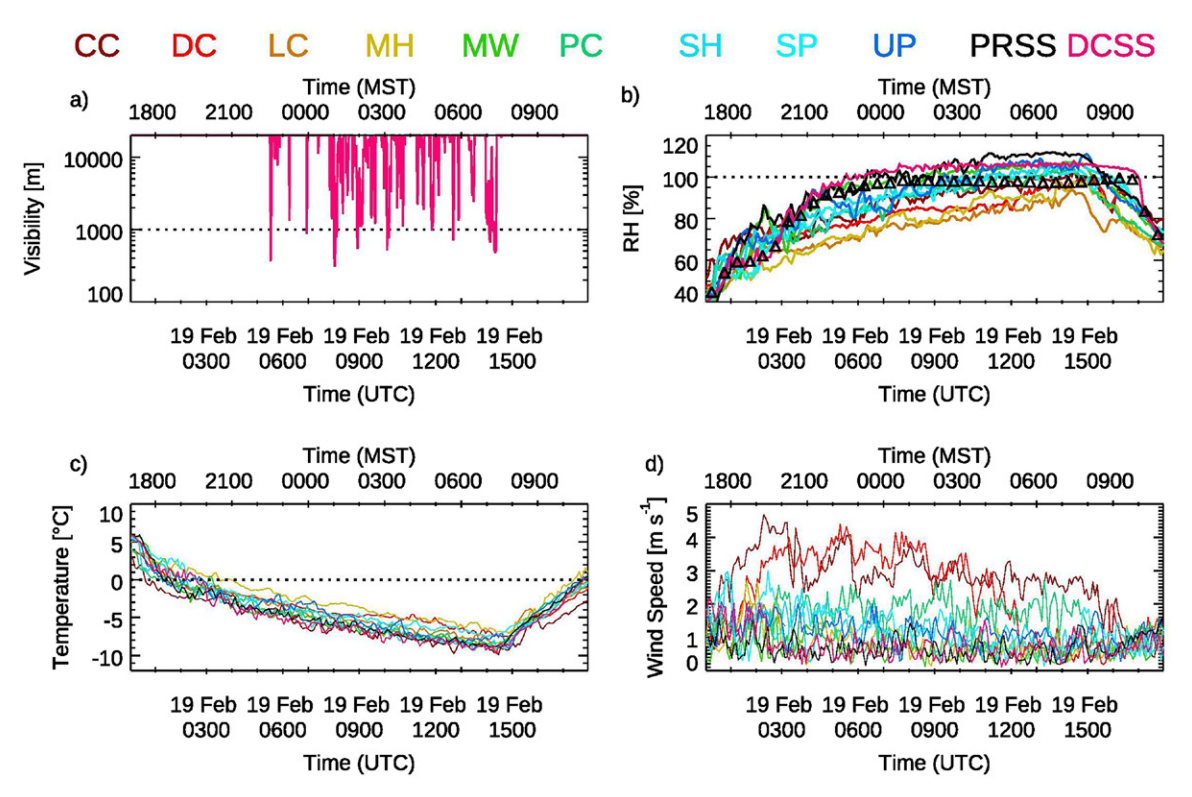


Fig. 6. Time series of meteorological conditions, including (a) visibility at the DC SS, as well as (b) relative humidity (RH) with respect to ice (lines), and the RH with respect to water (denoted by the triangle symbols) at DCSS at 2m. (c) Temperature and (d) wind speed at 2-m height observed during IOP 8, 19 Feb 2022 at all supersites and satellites sites.

the main moisture source was near the surface, and a drying throughout the early morning hours could be caused by fog formation and subsequent surface deposition of moisture to the surface. The IOP ended with the advection of drier and warmer air.

Figure 9 shows the time—height cross section of backscatter and linear depolarization ratio (LDR) from CL61 ceilometer at the DC SS sounding site, which indicates the formation and dissipation of the ephemeral fog layer during IOP 8. In general, a reduction in LDR during the formation of fog (see Fig. 9a for backscatter) is an indication that the physical composition of the observed fog is dominated by droplets. Complementary to the CL61 ceilometer observations, Fig. 10 shows a time series droplet size distribution (DSD) data obtained from the CDMS at DC SS. The DSD successfully observed several patches of ephemeral fog during IOP 8. The instrument is particularly good at capturing the full DSD at the high temporal resolution, which is important for short-lived ephemeral cold-fog events. More detailed microphysical properties of ice microphysical parameters such as ice water content (IWC), effective radius (Reff), and ice crystal number of concentration (Ni) (as illustrated in Fig. 11) were obtained from various microphysical sensors such as GCIP, Gondola (CDP and BCP), FM120, and CDMS, and OPC-N3 mentioned in the previous section.

Aerosol size distributions for IOP 8 (Fig. 12) clearly indicated the presence of fog. Starting at approximately 2000 UTC 18 February 2022, a decrease in aerosol concentration was observed by both the GRIMM and SMPS for over 5 h. This demonstrates scavenging and/or nucleation of the aerosols across the entire size distribution by the fog described above. The aerosols also demonstrated episodic decreases in concentration (e.g., 1400–1500 and 2000–2359 UTC) on 19 February as cold fog impacted the site.

In addition to characteristics of fog conditions, special measurements were also made to understand thermodynamic processes in the direct vicinity of the surface. For example, Fig. 13 shows the development of a lifted temperature minimum (LTM) during IOP 8. Causes for

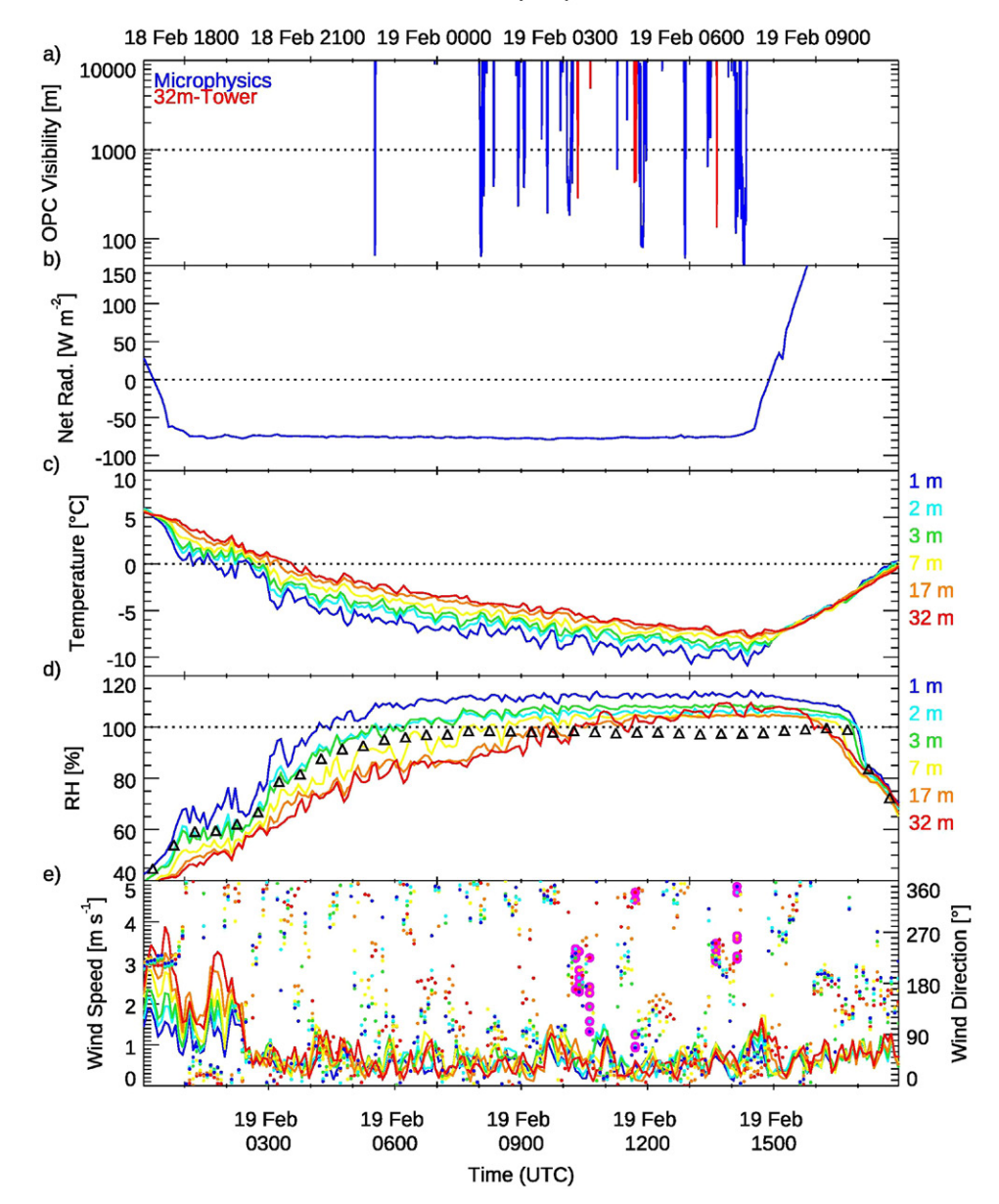


Fig. 7. Time series of meteorological conditions during IOP 8, 19 Feb 2022, including (a) visibility, (b) net radiation, (c) temperature, (d) relative humidity (RH) with respect to ice (lines), and the RH with respect to water (denoted by triangle symbols) at DCSS at 2 m, and (e) wind speed and wind direction. Color coding reflects six tower levels. Times when visibility at the DC SS flux tower site were below 1,000 m are highlighted in pink.

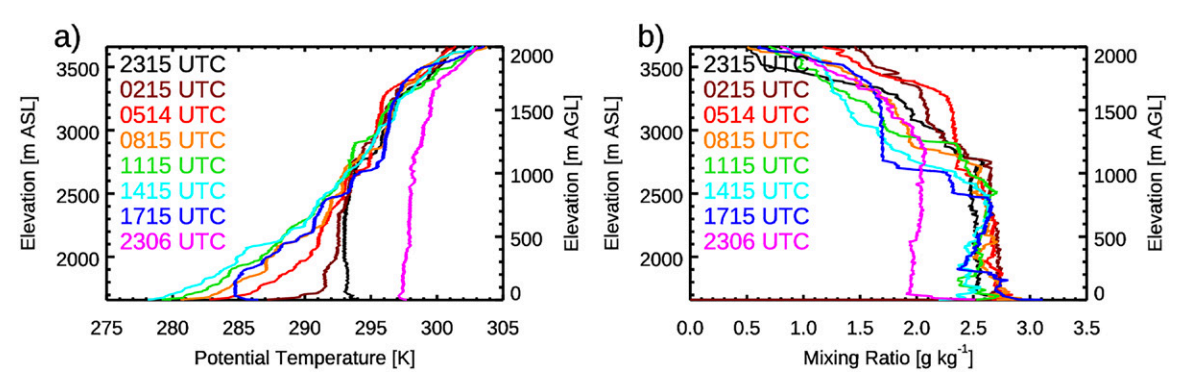


Fig. 8. (a) Potential temperature and (b) mixing ratio profiles in the lowest 2km AGL from soundings during IOP 8, 18–19 Feb 2022.

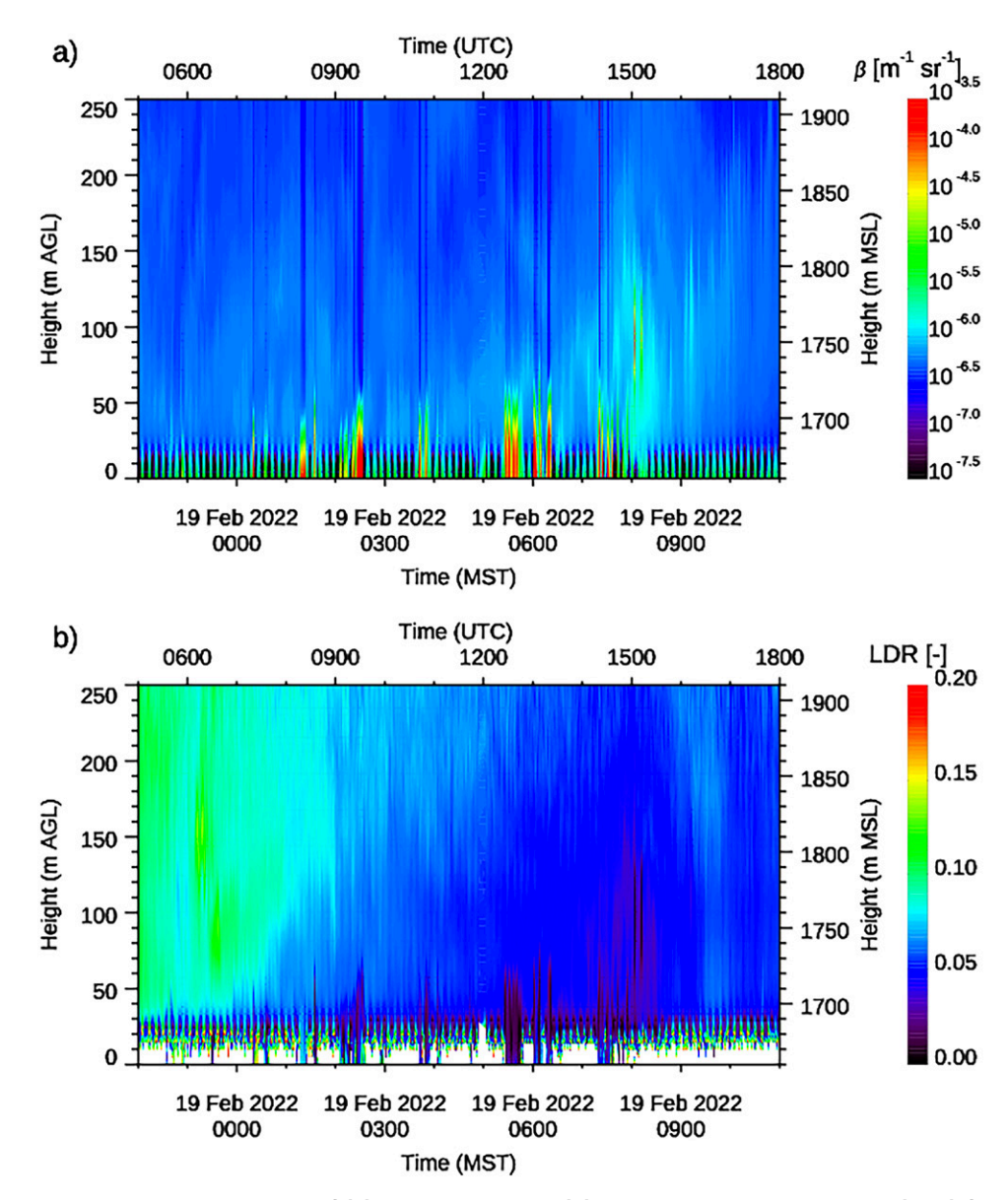


Fig. 9. Time-height cross section of (a) backscatter and (b) linear depolarization ratio (LDR) from CL61 ceilometer at the DC SS sounding site, indicating the formation and dissipation of the ephemeral fog layer during IOP 8, 18–19 Feb 2022. Note that periodic near-surface variations are instrument noise.

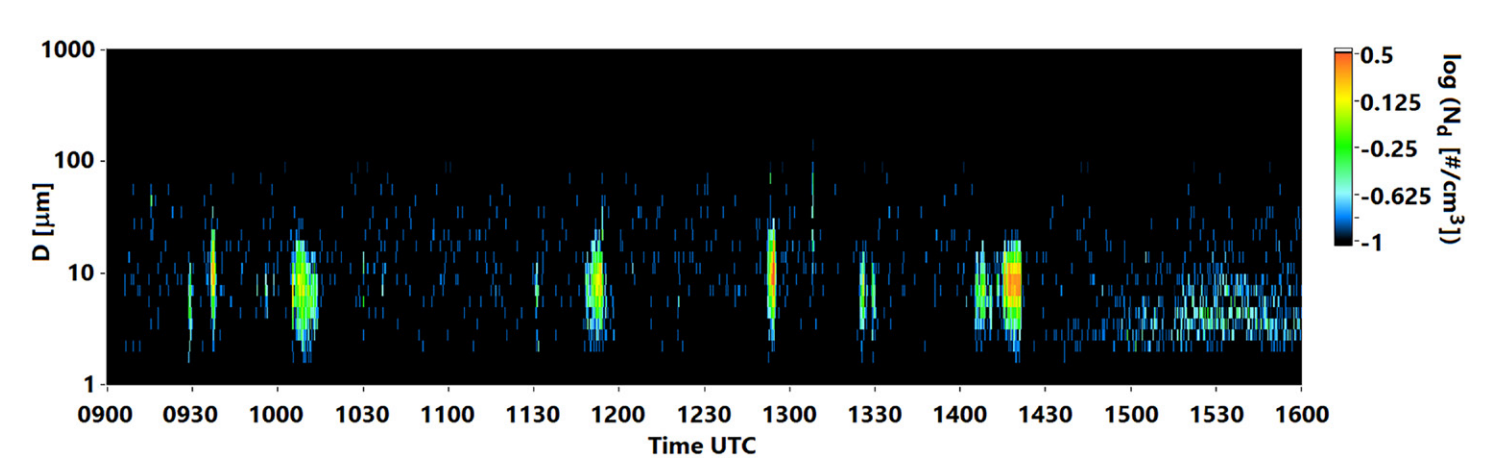


Fig. 10. Time series of DSD obtained during IOP 8 with the CDMS. A 5-s time constant (low-pass, 6 dB/oct filter) is applied to the original dataset (sampling rate: 1Hz) to reduce the noise. The vertical scale is a logarithm of droplet diameter D ( $\mu$ m). The intensity scale reflects a logarithm of droplet number concentration per histogram bin  $N_d$  (cm<sup>-3</sup>). Note that the artifacts present at about 1500–1600 UTC. These artifacts are caused by bright background illumination occurring during sunrise; they show up as erroneous sporadic counts in the smaller size bins.

this have rarely been discussed in the literature (Blay-Carreras et al. 2015). The CFACT measurements made it possible to relate this phenomenon with collocated observations of radiative heating and cooling profiles, aerosol abundance, and condensational warming.

More notably, CFACT provided a unique opportunity to integrate several instruments for understanding fog microphysical processes. Figure 14 illustrates the unique integration of several instruments at DC SS to understand cold-fog microphysical processes during IOP 9. The combination of the CL61 ceilometer's LDR,  $\beta$ ext from the scintillometer, and droplet size distribution from an OPC paints a clearer picture of

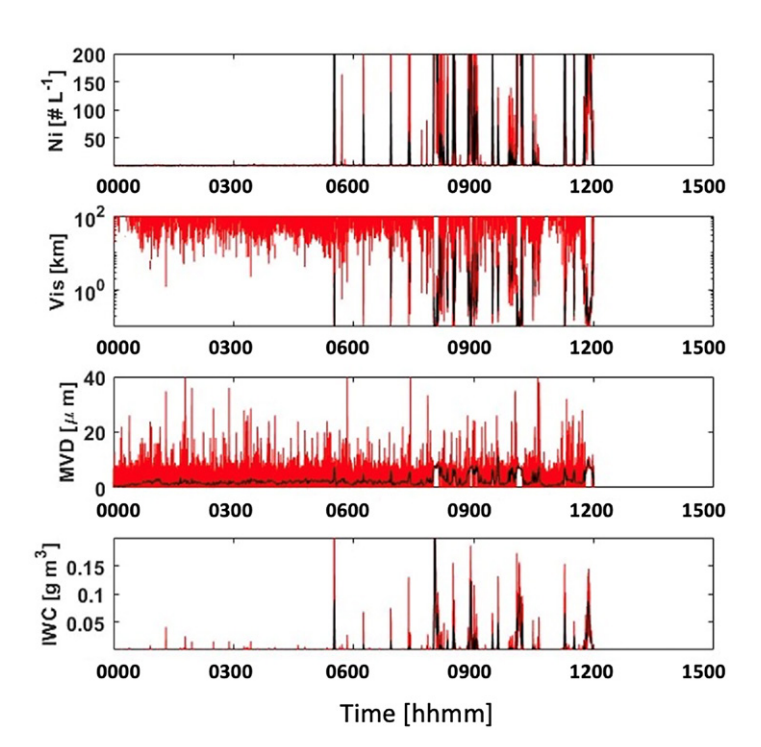


Fig. 11. FM120-based time series of ice crystal number of concentration (Ni), visibility, median volume diameter (MVD), and ice water content (IWC) for 1–50- $\mu$ m size range over 30 bins from 0000 to 1500 UTC 19 Feb 2022.

the types of particles that exist during cold fog (e.g., ice crystals or water droplets), which has clear implications for transportation safety beyond visibility such and icing conditions (Gultepe et al. 2019). The combination of spatially averaged and point measurements allows us to understand the heterogeneity of these short-lived periods of fog.

Specifically, during the periods highlighted in Fig. 14, two low-visibility periods exist where a relationship between LDR and  $\beta$ ext can be seen. Since microwave radiation is attenuated more by liquid water than by ice, a negative correlation between  $\beta$ ext and LDR is found as expected. When LDR = 0, the atmosphere is filled with water droplets, and an increase in LDR shows an increase in ice particles in the air as well as an increase in the complexity of the crystals. Using additional information from the GCIP (Fig. 15) at 7.5–960- $\mu$ m size range, the amount of liquid water in the air can be determined and the mixed-phase conditions interpreted (i.e., with the liquid water amount of 0.12 g m<sup>-3</sup> and the ice water amount of  $0.10 \,\mathrm{g}\,\mathrm{m}^{-3}$  during these periods); that is, we can identify periods when pure water or pure ice exist. The highlighted period in Fig. 14 from 0620 to 0640 MST 24 February 2022 (local time) shows  $\beta$ ext as visibility drops and LDR decreases, leading us to suspect that during dense fog, there may be supercooled water droplets; then, upon fog dissipation, more ice crystals form. Even during the short, highlighted period from 0740 to 0745 MST 24 February 2022 (local time), there is a drop in LDR that is associated with a drop in visibility. There is no clear signal from  $\beta$ ext, which is not unexpected since the instruments were separated by several hundred meters, and IOP 9 is characterized by patchy fog.

#### **CFACT model simulations at the subkilometer scale**

During the CFACT field campaign, fog prediction was challenging, as conventional NWP can only guide synoptic and mesoscale forecasts without much local- and small-scale information needed for fog prediction. An Advanced Research version of the Weather Research and Forecasting (WRF) Model (Skamarock et al. 2019) version 4.3 was used during the field campaign to produce real-time high-resolution local forecasts, with the intention to use it as a tool for postfield process studies and for identifying NWP model deficiencies.

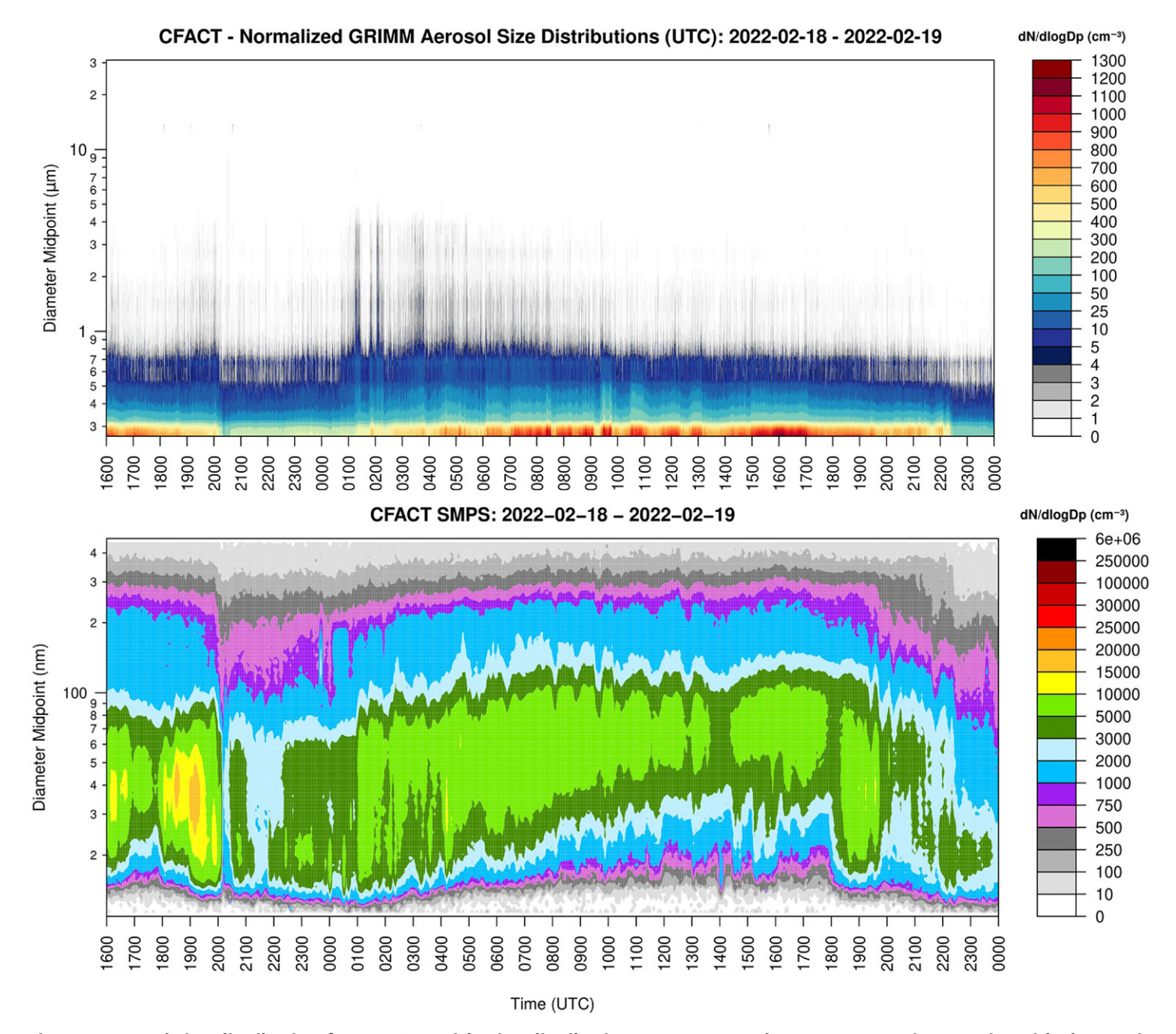


Fig. 12. Aerosol size distribution for IOP 8. Particle size distributions are presented as a concentration matrix, with the x axis representing time and the y axis representing the particle size. The colors represent the concentration (unit:  $dN/d\log Dp$ ). (top) GRIMM distribution (0.5–30  $\mu$ m). (bottom) SMPS distribution (8–450 nm).

Four one-way nested domains were used, with horizontal grid resolutions of 12 km, 4 km, 1.33 km and 444.4 m, respectively. The innermost domain (444.4 m) focused on Heber City and its vicinity; 72 h forecasts were made daily with initial time at 0000 and 1200 UTC using initial and boundary conditions derived from the NCEP NAM analysis and forecasts. Forecast results indicate that the WRF high-resolution (444.4 m) forecasts captured most of the near-surface saturation situations, temperature trends, and low wind conditions, although errors are seen when compared with observations (e.g., Fig. 16). The WRF forecasts can distinguish the meteorological conditions at the different stations over Heber Valley (Figs. 16a–c). Due to the lack of an accurate visibility algorithm and forecast errors in the near-surface and boundary layer atmosphere conditions, predicting fog events is still challenging.

As part of the CFACT modeling study, Li and Pu (2022) performed large-eddy simulations (LES; at ~10-m grid spacing) using WRF (WRF-LES). They concluded that a horizontal

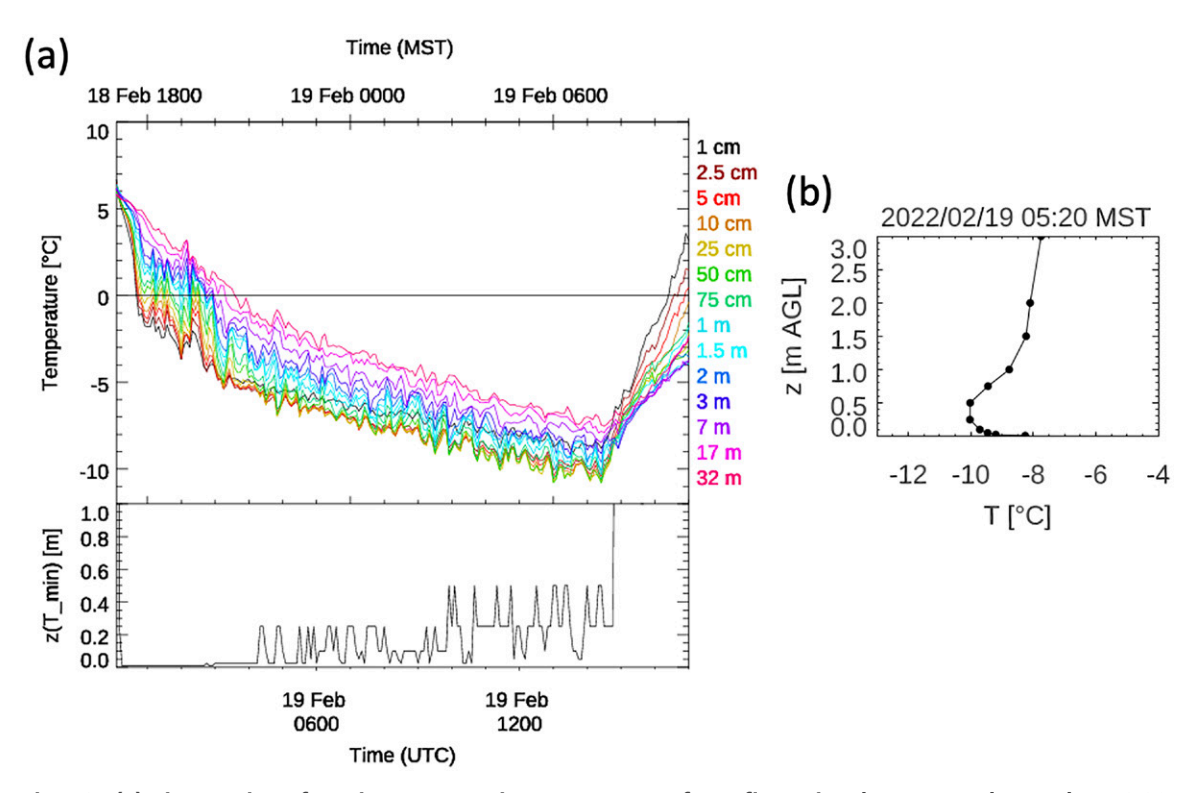


Fig. 13. (a) Time series of 5-min-average air temperatures from fine wire thermocouples at the DC SS, 18–19 Feb 2022, along with the height of minimum temperature. After initial near-surface cooling, the temperate minimum lifts away from the surface, and the lowest temperatures are observed around 50 cm above the ground. (b) Near-surface 5-min-average temperature profile below 3 m at 0520 MST 19 Feb 2022 illustrating the LTM.

resolution of 100 m or less is necessary for accurate fog simulations. In Li and Pu (2022), a winter fog case that occurred on 16 January 2015 in Heber Valley was successfully simulated by WRF large-eddy simulations at 40-m horizontal grid resolution. Specifically, the simulation results indicated that large-scale turbulent eddies prevailed and dominated the mixing in the PBL. The WRF large-eddy simulation at the 40-m grid scale successfully simulated the effects of turbulence, while the simulation at a 1-km grid resolution failed to reveal the turbulence. The combination of turbulence mixing effects, mountain–valley flow, and ultracold valley temperatures led to fog formation in the LES simulation. The omission of turbulent eddies in the PBL parameterization scheme (in the kilometer-scale simulations) resulted in weak mixing

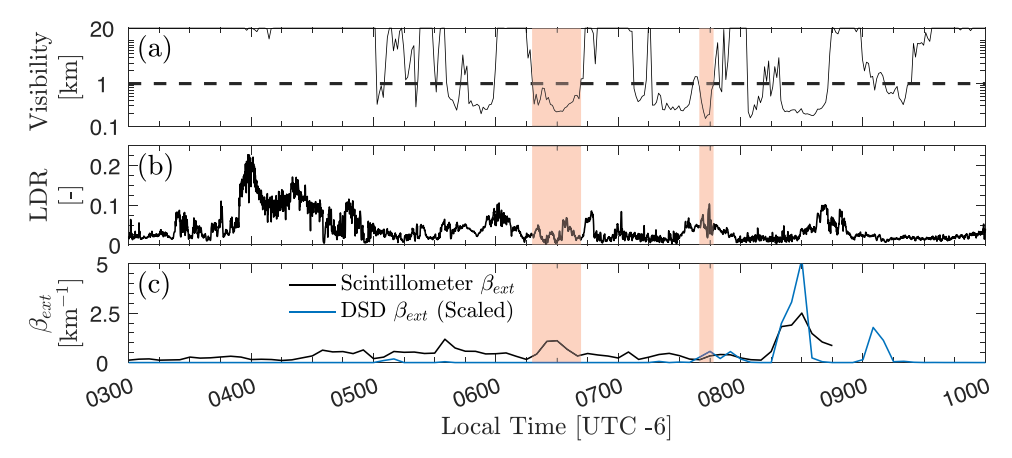


Fig. 14. Data from DC SS site on 24 Feb during IOP 9: (a) visibility from a Vaisala PWD, (b) linear depolarization ratio (LDR) from Vaisala CL61 (40-m gate), and (c) extinction coefficient at 1.86 mm calculated from the RPG-MWS160 and the drop size distribution from the AlphaSense OPC-N3 and Parsivel OTT at the 32-m tower. Highlighted areas show periods of interest discussed.

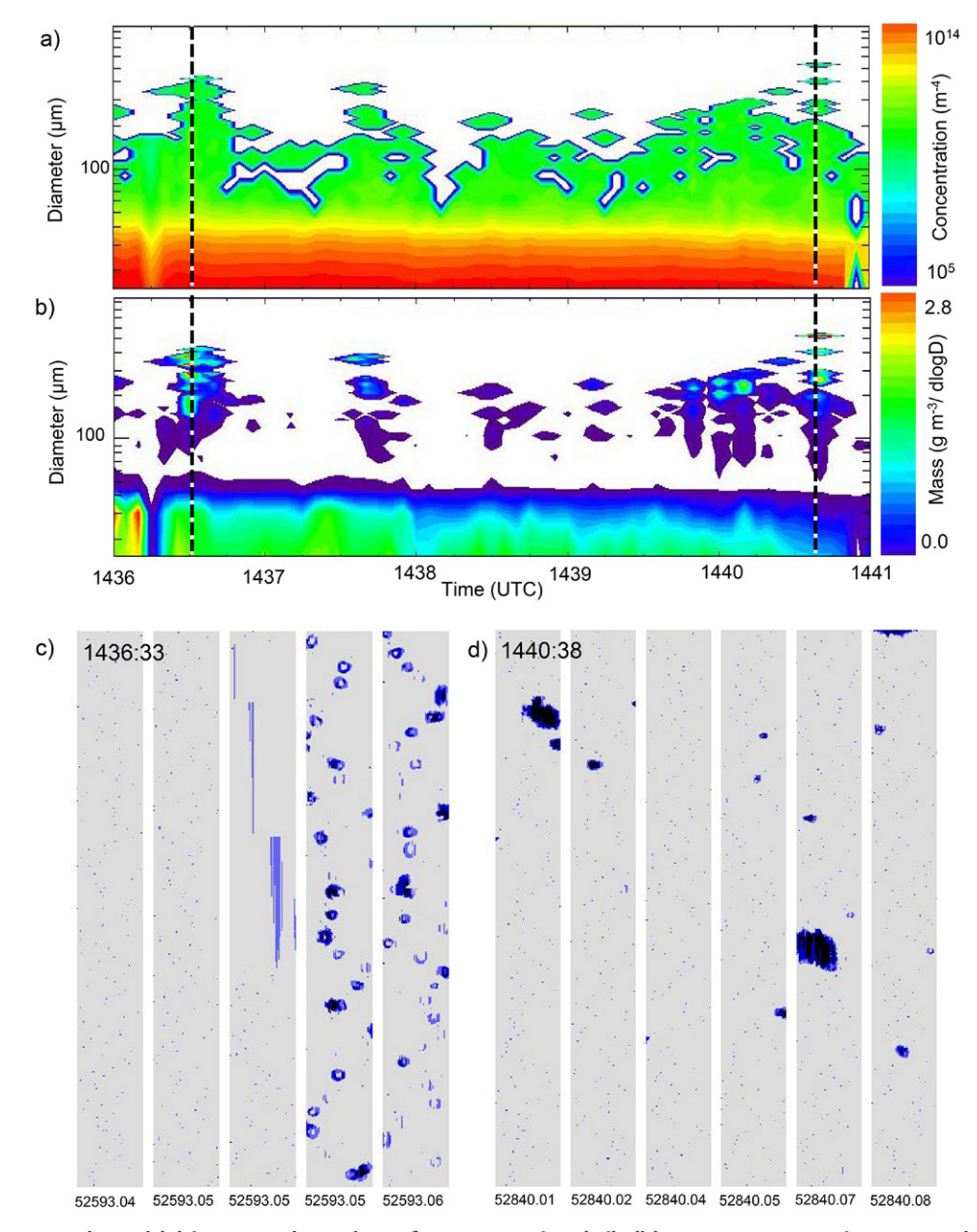


Fig. 15. GCIP-based (a) ice crystal number of concentration (Ni), (b) mass concentration spectral density time series for the ice-fog case on 24 Feb. (c),(d) Particle habits for the 24 Feb 2022 case from 1436 to 1440 UTC [indicated by vertical lines in (a) and (b)]. Dots in (c) show supercooled droplets/frozen particles and some rimed particles on the right, which have a size of about 300  $\mu$ m at 1440 UTC. Note that the width of each gray strip in (c) has a physical dimension of 940  $\mu$ m.

in the PBL and weakened the near-surface air cooling, resulting in the eventual failure to reproduce the fog in the numerical simulation (see details in Li and Pu 2022).

During the CFACT campaign, the 32-m tower data from NCAR EOL ISFS were extremely useful for examining boundary layer turbulence effects on fog formation. Consistent with the findings from the LES by Li and Pu (2022), observations indicate that turbulence affects fog formation and its life cycle. For instance, Fig. 17 shows that turbulence intensity, represented by turbulence kinetic energy (TKE), was large before fog onset and during the fog dissipation but small during the fog event.

### Summary and ongoing/future research

The Cold Fog Amongst Complex Terrain (CFACT) field campaign conducted in Utah's Heber Valley provided a dense network of observations of meteorological parameters and utilized

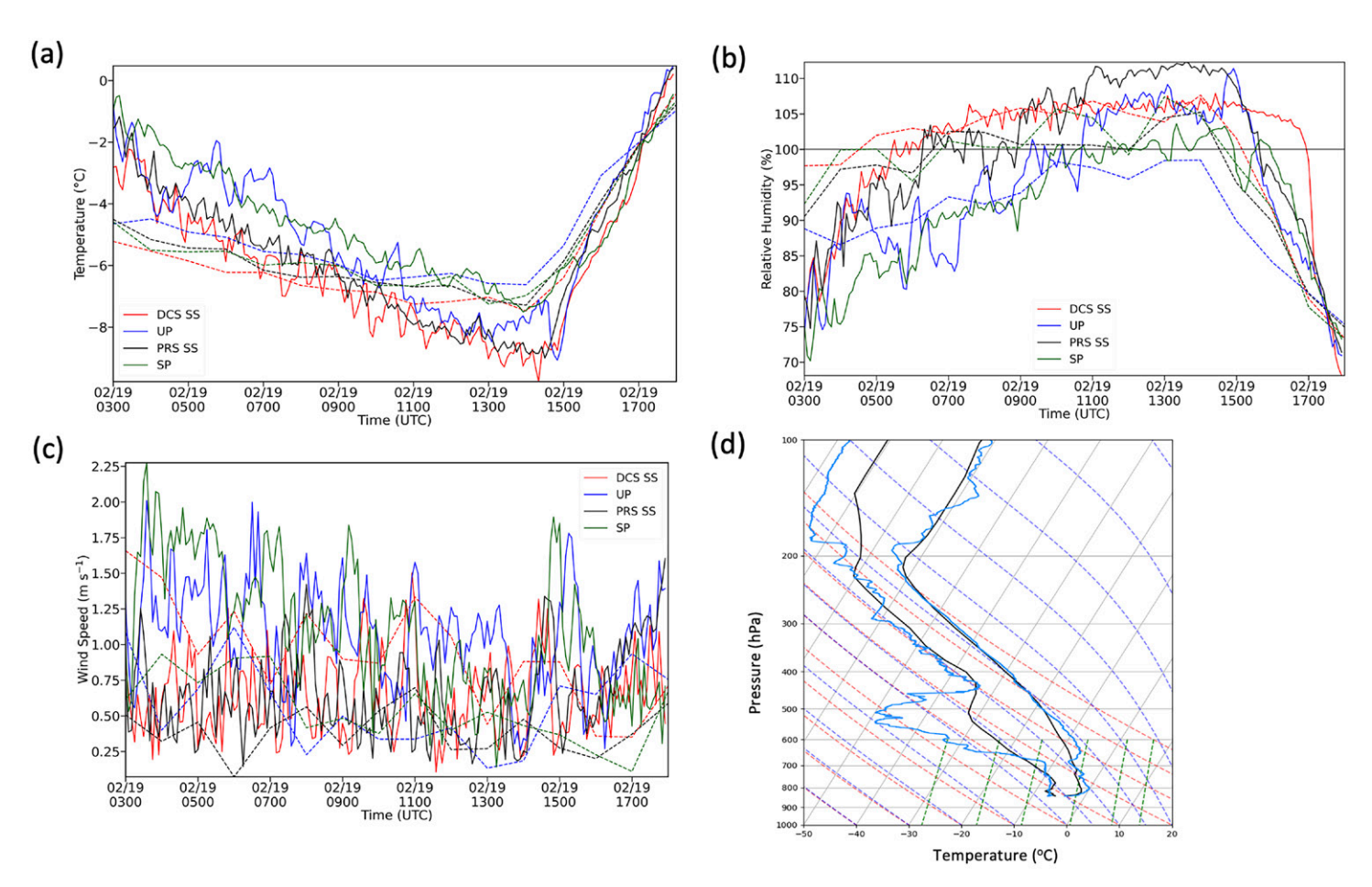


Fig. 16. WRF Model predicted (a) temperature, (b) relative humidity with respect to ice, and (c) wind speed at 2-m height (dashed lines) initialized from 0000 UTC 18 Feb during the IOP 8 against observations (solid lines) for two satellite sites and two supersites. (d) Comparison between radiosonde observations (blue) and WRF-simulated sounding (black) at 0500 UTC 19 Feb 2022 during IOP 8 at DC SS.

NWP model simulations to investigate the life cycle of fog and stable boundary layer processes. During the 7-week CFACT field campaign, nine intensive observation periods yielded a dataset that included high-frequency radiosonde profiles, tethered balloon profiles, remotely sensed thermodynamic and wind profiles, numerous surface meteorological observations, and microphysical and aerosol measurements. Due to the drought in the western United States in

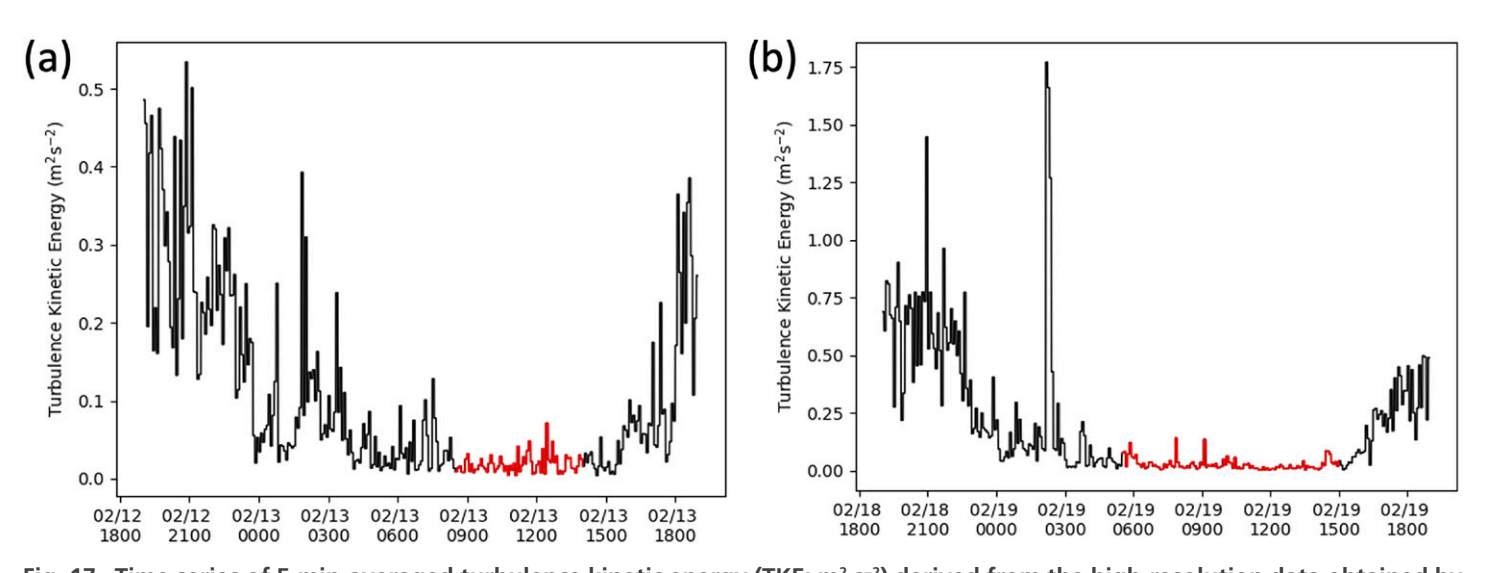


Fig. 17. Time series of 5-min-averaged turbulence kinetic energy (TKE; m² s-²) derived from the high-resolution data obtained by the EOL ISFS tower at DC SS during (a) IOP 6 and (b) IOP 8 at 32-m height. Red denotes the TKE during the period of fog.

2022, and despite observing cold-air-pool conditions regularly, CFACT did not observe any persistent deep fog events associated with persistent cold-air pools that regularly form in higher-elevation Intermountain West basins. The observed fog events were limited to highly spatially heterogeneous ephemeral fog and ice fog events. However, since ephemeral fog and ice fog are extremely difficult to detect, model, and forecast, CFACT provided unprecedented datasets to understand both types of fog and validate the NWP model. Meanwhile, the variety of nonfog IOPs provided valuable observations for understanding near-surface inversion, ice crystal formation, moisture advection and transportation, and stable boundary layers over complex terrain, all of which are essential factors related to fog formation. Comprehensive studies are ongoing for an improved understanding of cold fog over complex terrain.

More importantly, since Heber Valley is a small-scale valley, the observations from the two CFACT supersites, eight low-cost stations, and nine satellite sites provide critical high-resolution observations to validate and improve current and next-generation (i.e., subkilometer scale) NWP models. In a recent study, Li and Pu (2021) demonstrated the feasibility of using LES high-resolution data to improve the vertical eddy-diffusivity parameterization within the WRF PBL scheme. With observations at high sampling frequencies representing the near-surface atmospheric conditions, PBL, turbulence, microphysical properties, and visibility, the data collected from CFACT provide a unique opportunity to validate and improve the NWP model physical parameterization scheme and develop effective visibility algorithms. Moreover, the available CFACT high-resolution meteorological observations, along with the soil moisture and snow observations during CFACT, are helpful for developing fine-scale atmospheric data assimilation and the coupled land–atmosphere data assimilation (e.g., Lin and Pu 2019, 2020; Zhang and Pu 2019) for improved near-surface weather prediction, including cold-fog forecasting. Various comprehensive studies are presently underway for numerical model validation, improvement, and data assimilation to improve cold-fog prediction.

**Acknowledgments.** We would like to acknowledge the operational, technical, and scientific support provided by NCAR's Earth Observing Laboratory, sponsored by the National Science Foundation. We thank the land owners, especially Grant Kohler and Wasatch State Park for allowing us to place instruments on their property. We are grateful to John Komar and Martin Agelin-Chaab from Ontario Technical University, for their resources to support the microphysical instrument suite. We are also grateful to the following students and postdocs who participated in the fieldwork during the CFACT field project: Johnathan Stoddard, Matt DeMaria, Pauline Kneller, Angelina Miller, Zach Ruble, Ben Silberman, Travis Morrison, Savanna Wolvin, Michael Wasserstein, Nancy Sohlberg, Grace Liu, Nic Hofmann, Haley Scott, Zac Claerhout, Noah Hirshorn, Bayasal Baterdene, Pete Gombert, and Michael Pletcher. Forecast support from the NWS local office led by Darren van Cleave is greatly appreciated. CFACT science panel members Bergot Thierry (Meteo-France), Yansen Wang (U.S. Army Research Laboratory), Vijay Tallapragada (NOAA/NCEP), Matt Jeglum (NOAA/NWS Western Region Headquarters), Darren van Cleave (NOAA/NWS Weather Forecast Office at Salt Lake City), and Chris Pennell (Utah Division of Air Quality) are acknowledged for their input and useful discussion of field and science planning. The high-performance computing support from Cheyenne (DOI:10.5065/D6RX99HX) provided by NCAR's Computational and Information Systems Laboratory, sponsored by the National Science Foundation and the University of Utah's Center for High-Performance Computing is greatly appreciated. This project is supported by NSF Award 2049100. The NSF Physical and Dynamic Meteorology program managers, the NSF LAOF program, and the NCAR EOL managers are all appreciated.

**Data availability statement.** The CFACT field campaign catalog and observations are available at a data repository managed by NCAR's Earth Observing Laboratory at <a href="https://catalog.eol.ucar.edu/cfact">https://catalog.eol.ucar.edu/cfact</a>. The PIs' data from the University of Utah and Ontario Technical University (OntTecU) are available upon request.

## References

- Bergot, T., and D. Guédalia, 1994a: Numerical forecasting of radiation fog. Part I: Numerical model and sensitivity tests. *Mon. Wea. Rev.*, **122**, 1218–1230, https://doi.org/10.1175/1520-0493(1994)122<1218:NFORFP>2.0.CO;2.
- ——, and ——, 1994b: Numerical forecasting of radiation fog. Part II: A comparison of model simulation with several observed fog events. *Mon. Wea. Rev.*, **122**, 1231–1246, https://doi.org/10.1175/1520-0493(1994)122<1231:NFORFP> 2.0.CO;2.
- ——, D. Carrer, J. Noilhan, and P. Bougeault, 2005: Improved site-specific numerical prediction of fog and low clouds: A feasibility study. Wea. Forecasting, 20, 627–646, https://doi.org/10.1175/WAF873.1.
- Blay-Carreras, E., E. R. Pardyjak, D. Pino, S. W. Hoch, J. Cuxart, D. Martínez, and J. Reuder, 2015: Lifted temperature minimum during the atmospheric evening transition. *Atmos. Chem. Phys.*, **15**, 6981–6991, https://doi.org/10.5194/acp-15-6981-2015.
- Bott, A., U. Sievers, and W. Zdunkowski, 1990: A radiation fog model with a detailed treatment of the interaction between radiative transfer and fog microphysics. J. Atmos. Sci., 47, 2153–2166, https://doi.org/10.1175/1520-0469(1990)047<2153:ARFMWA>2.0.CO;2.
- Chachere, C. N., and Z. Pu, 2018: Numerical simulations of an inversion fog event in the Salt Lake valley during the MATERHORN-Fog field campaign. *Pure Appl. Geophys.*, **176**, 2139–2164, https://doi.org/10.1007/s00024-018-1770-8.
- Clayton, J., T. Brosten, K. Sutcliffe, D. Eiriksson, J. Burly, and D. Neff, 2022: Utah water supply outlook report. NRCS Rep., 65 pp.
- Colman, B., K. Cook, and B. J. Snyder, 2013: Numerical weather prediction and weather forecasting in complex terrain. *Mountain Weather Research and Forecasting*, F. K. Chow, S. F. J. De Wekker, and B. J. Snyder, Eds., Springer Netherlands, 655–692, https://doi.org/10.1007/978-94-007-4098-3.
- Fernando, H. J. S., and Coauthors, 2015: The MATERHORN: Unraveling the intricacies of mountain weather. *Bull. Amer. Meteor. Soc.*, **96**, 1945–1967, https://doi.org/10.1175/BAMS-D-13-00131.1.
- ——, and Coauthors, 2019: The Perdigão: Peering into microscale details of mountain winds. *Bull. Amer. Meteor. Soc.*, **100**, 799–819, https://doi.org/10. 1175/BAMS-D-17-0227.1.
- Forthun, G. M., M. B. Johnson, W. G. Schmitz, J. Blume, and R. J. Caldwell, 2006: Trends in fog frequency and duration in the southeast United States. *Phys. Geogr.*, **27**, 206–222, https://doi.org/10.2747/0272-3646.27.3.206.
- Gultepe, I., and J. A. Milbrandt, 2010: Probabilistic parameterizations of visibility using observations of rain precipitation rate, relative humidity, and visibility. J. Appl. Meteor. Climatol., 49, 36–46, https://doi.org/10.1175/2009JAMC1927.1.
- ——, and Coauthors, 2007a: Fog research: A review of past achievements and future perspectives. *Pure Appl. Geophys.*, **164**, 1121–1159, https://doi.org/ 10.1007/s00024-007-0211-x.
- ——, M. Pagowski, and J. Reid, 2007b: A satellite-based fog detection scheme using screen air temperature. Wea. Forecasting, 22, 444–456, https://doi. org/10.1175/WAF1011.1.
- —, G. Pearson, J. A. Milbrandt, B. Hansen, S. Platnick, P. Taylor, M. Gordon, and J. P. Oakley, 2009: The Fog Remote Sensing and Modeling (FRAM) field project. *Bull. Amer. Meteor. Soc.*, **90**, 341–360, https://doi.org/10.1175/2008 BAMS2354.1.
- ——, and Coauthors, 2014: Ice fog in Arctic during FRAM-IF project: Aviation and nowcasting applications. *Bull. Amer. Meteor. Soc.*, **95**, 211–226, https://doi.org/10.1175/BAMS-D-11-00071.1.
- ——, and Coauthors, 2015: A review on ice fog measurements and modeling. Atmos. Res., 151, 2–19, https://doi.org/10.1016/j.atmosres.2014.04.014.
- —, and Coauthors, 2016: An overview of the MATERHORN fog project: Observations and predictability. *Pure Appl. Geophys.*, **173**, 2983–3010, https://doi.org/10.1007/s00024-016-1374-0.
- ——, A. J. Heymsfield, M. Gallagher, L. Ickes, and D. Baumgardner, 2017: Ice fog: The current state of knowledge and future challenges. *Ice Formation and Evolution in Clouds and Precipitation: Measurement and Modeling Challenges*,

- *Meteor. Monogr.*, No. 58, Amer. Meteor. Soc., https://doi.org/10.1175/AMS MONOGRAPHS-D-17-0002.1.
- ——, and Coauthors, 2019: A review of high impact weather for aviation meteorology. *Pure Appl. Geophys.*, **176**, 1869–1921, https://doi.org/10.1007/ s00024-019-02168-6.
- ——, A. J. Heymsfield, and M. Gallagher, 2020: Arctic ice fog: Its microphysics and prediction. *Physics and Chemistry of the Arctic Atmosphere*, A. Kokhanovsky and C. Tomasi, Eds., Springer, 361–414.
- ——, and Coauthors, 2021: A review of coastal fog microphysics during C-FOG. *Bound.-Layer Meteor.*, **181**, 227–265, https://doi.org/10.1007/s10546-021-00659-5.
- Gunawardena, N., E. R. Pardyjak, R. Stoll, and A. Khadka, 2018: Development and evaluation of an open-source low-cost distributed sensor network for environmental monitoring applications. *Meas. Sci. Technol.*, **29**, 024008, https://doi.org/10.1088/1361-6501/aa97fb.
- Hallar, A. G., G. Chirokova, I. B. McCubbin, T. H. Painter, C. Wiedinmyer, and C. Dodson, 2011: Atmospheric bioaerosols transported via dust storms in western United States. *Geophys. Res. Lett.*, 38, L17801, https://doi.org/10. 1029/2011GL048166.
- ——, R. Petersen, I. B. McCubbin, D. Lowenthal, S. Lee, E. Andrews, and F. Yu, 2016: Climatology of new particle formation and corresponding precursors at storm peak laboratory. *Aerosol Air Qual. Res.*, 16, 816–826, https://doi.org/10.4209/aaqr.2015.05.0341.
- Hang, C., and Coauthors, 2016: A case study of the mechanisms modulating the evolution of valley fog. *Pure Appl. Geophys.*, **173**, 3011–3030, https://doi. org/10.1007/s00024-016-1370-4.
- Hodges, D., and Z. Pu, 2016: The climatology, frequency, and distribution of cold season fog events in northern Utah. *Pure Appl. Geophys.*, **173**, 3197–3211, https://doi.org/10.1007/s00024-015-1187-6.
- Kapoor, P., 2019: Over 10,000 lives lost in fog-related road crashes. *Times of India*, 5 January, https://timesofindia.indiatimes.com/india/over-10000-lives-lost-infog-related-roadcrashes/articleshow/67391588.cms.
- Kloesel, K. A., 1992: A 70-year history of marine stratocumulus cloud field experiments off the coast of California. *Bull. Amer. Meteor. Soc.*, 73, 1581–1585, https://doi.org/10.1175/1520-0477(1992)073<1581:AYHOMS>2.0.CO;2.
- Kunkel, B. A., 1984: Parameterization of droplet terminal velocity and extinction coefficient in fog models. J. Climate Appl. Meteor., 23, 34–41, https://doi.org/ 10.1175/1520-0450(1984)023<0034:PODTVA>2.0.CO;2.
- Lareau, N. P., E. Crosman, C. D. Whiteman, J. D. Horel, S. W. Hoch, W. O. J. Brown, and T. W. Horst, 2013: The Persistent Cold-Air Pool Study. *Bull. Amer. Meteor. Soc.*, 94, 51–63, https://doi.org/10.1175/BAMS-D-11-00255.1.
- Leipper, D. F., 1994: Fog on the U.S. West Coast: A review. *Bull. Amer. Meteor. Soc.*, **75**, 229–240, https://doi.org/10.1175/1520-0477(1994)075<0229:FOT UWC>2.0.CO;2.
- Li, X., and Z. Pu, 2021: Vertical eddy diffusivity parameterization based on a large eddy simulation and its impact on prediction of hurricane landfall. *Geophys. Res. Lett.*, **48**, e2020GL090703, https://doi.org/10.1029/2020GL090703.
- —, and —, 2022: Turbulence effects on the formation of cold fog over complex terrain with large-eddy simulation. *Geophys. Res. Lett.*, **49**, e2022GL098792, https://doi.org/10.1029/2022GL098792.
- Lin, L.-F., and Z. Pu, 2019: Examining the impact of SMAP soil moisture retrievals on short-range weather prediction under weakly and strongly coupled data assimilation with WRF-Noah. *Mon. Wea. Rev.*, **147**, 4345–4366, https://doi.org/10.1175/MWR-D-19-0017.1.
- ——, and ——, 2020: Improving near-surface short-range weather forecasts using strongly coupled land—atmosphere data assimilation with GSI-EnKF. *Mon. Wea. Rev.*, **148**, 2863–2888, https://doi.org/10.1175/MWR-D-19-0370.1.
- Liu, Y., and Coauthors, 2008a: The operational mesogamma-scale analysis and forecast system of the U.S. Army Test and Evaluation Command. Part I: Overview of the

- modeling system, the forecast products, and how the products are used. *J. Appl. Meteor. Climatol.*, **47**, 1077–1092, https://doi.org/10.1175/2007JAMC1653.1.
- —, and Coauthors, 2008b: The operational mesogamma-scale analysis and fore-cast system of the U.S. Army Test and Evaluation Command. Part II: Interrange comparison of the accuracy of model analyses and forecasts. J. Appl. Meteor. Climatol., 47, 1093–1104, https://doi.org/10.1175/2007JAMC1654.1.
- Mass, C. F., D. Ovens, K. Westrick, and B. A. Colle, 2002: Does increasing horizontal resolution produce more skillful forecasts? *Bull. Amer. Meteor. Soc.*, 83, 407–430, https://doi.org/10.1175/1520-0477(2002)083<0407:DIHRPM>2.3.CO;2.
- Massey, J. D., W. J. Steenburgh, S. W. Hoch, and J. C. Knievel, 2014: Sensitivity of near-surface temperature forecasts to soil properties over a sparsely vegetated dryland region. J. Appl. Meteor. Climatol., 53, 1976–1995, https://doi. org/10.1175/JAMC-D-13-0362.1.
- Noonkester, V. R., 1979: Coastal marine fog in Southern California. *Mon. Wea. Rev.*, **107**, 830–851, https://doi.org/10.1175/1520-0493(1979)107<0830:CM FISC>2.0.CO:2.
- Paci, A., and Coauthors, 2016: La campagne Passy-2015: Dynamique atmosphérique et qualité de l'air dans la vallée de l'Arve. *Pollut. Atmos.*, 231–232, https://doi.org/10.4267/pollution-atmospherique.5903.
- Pagowski, M., I. Gultepe, and P. King, 2004: Analysis and modeling of an extremely dense fog event in southern Ontario. J. Appl. Meteor., 43, 3–16, https://doi.org/10.1175/1520-0450(2004)043<0003:AAMOAE>2.0.CO;2.
- Price, J., and Coauthors, 2018: LANFEX: A field and modeling study to improve our understanding and forecasting of radiation fog. *Bull. Amer. Meteor. Soc.*, **99**, 2061–2077, https://doi.org/10.1175/BAMS-D-16-0299.1.
- Pu, Z., 2017: Surface data assimilation and near-surface weather prediction over complex terrain. *Data Assimilation for Atmospheric, Oceanic and Hydrologic Applications*, Vol. III, S. K. Park and L. Xu, Eds., Springer, 219–240.

- —, C. N. Chachere, S. W. Hoch, E. R. Pardyjak, and I. Gultepe, 2016: Numerical prediction of cold season fog events over complex terrain: The performance of the WRF Model during MATERHORN-Fog and early evaluation. *Pure Appl. Geophys.*, **173**, 3165–3186, https://doi.org/10.1007/s00024-016-1375-z.
- Skamarock, W. C., and Coauthors, 2019: A description of the Advanced Research WRF Model version 4. NCAR Tech. Note NCAR/TN-556+STR, 145 pp., https:// doi.org/10.5065/1dfh-6p97.
- Smith, D. K. E., I. A. Renfrew, S. R. Dorling, J. D. Price, and I. A. Boutle, 2020: Sub-km scale numerical weather prediction model simulations of radiation fog. *Quart. J. Roy. Meteor. Soc.*, **147**, 746–763, https://doi.org/10.1002/qj.3943.
- Tardif, R., and R. M. Rasmussen, 2007: Event-based climatology and typology of fog in the New York City region. J. Appl. Meteor. Climatol., 46, 1141–1168, https://doi.org/10.1175/JAM2516.1.
- Van Den Bossche, M., and S. De Wekker, 2016: Spatiotemporal variability of surface meteorological variables during fog and no-fog events in the Heber Valley, UT: Selected case studies from MATERHORN-Fog. *Pure Appl. Geophys.*, 173, 3031–3048, https://doi.org/10.1007/s00024-016-1352-6.
- Zhang, F., and Z. Pu, 2019: Sensitivity of numerical simulations of near-surface atmospheric conditions to snow depth and surface albedo during an ice fog event over Heber Valley. J. Appl. Meteor. Climatol., 58, 797–811, https://doi. org/10.1175/JAMC-D-18-0064.1.
- Zhang, H., Z. Pu, and X. Zhang, 2013: Examination of errors in near-surface temperature and wind from WRF numerical simulations in regions of complex terrain. Wea. Forecasting, 28, 893–914, https://doi.org/10.1175/WAF-D-12-00109.1.
- Zhou, B., and J. Du, 2010: Fog prediction from a multimodel mesoscale ensemble prediction system. *Wea. Forecasting*, **25**, 303–322, https://doi.org/10.1175/2009WAF2222289.1.